A Warm-Bin–Cold-Bulk Hybrid Cloud Microphysical Model*

RYO ONISHI AND KEIKO TAKAHASHI

Earth Simulator Center, Japan Agency for Marine-Earth Science and Technology, Yokohama, Japan

(Manuscript received 23 June 2011, in final form 29 October 2011)

ABSTRACT

This study describes a newly developed bin–bulk hybrid cloud microphysical model named MSSG-Bin, which has been implemented in the Multi-Scale Simulator for the Geoenvironment (MSSG). In the hybrid approach, a spectral bin scheme is used for liquid droplets, while a bulk scheme is used for solid particles. That is, the expensive but more reliable spectral bin scheme treats the relatively well-understood physics of the liquid phase, and the computationally efficient but less robust bulk scheme is used to treat the poorly understood physics of the ice phase. In the bulk part, the prognostic variables are the mixing ratios of cloud ice, snow, and graupel and the number density of cloud ice particles. The bulk component is consistent with MSSG-Bulk, which is a conventional bulk model implemented in MSSG. One-dimensional kinetic simulations and three-dimensional cloud simulations have confirmed the reliability of MSSG-Bin for warm clouds, free from the approximations made in bulk parameterizations, and its applicability to cold clouds, without the significant additional costs required for a bin treatment of the ice phase. Compared with MSSG-Bulk, MSSG-Bin with 33 bins requires 8.3 times more floating-point operations for a one-dimensional shallow convection case, and 4.9 times more for a three-dimensional shallow convection case. Present results have shown the feasibility of using this model for a 25-m-resolution simulation of shallow cumulus on a $512 \times 512 \times 200$ grid.

1. Introduction

Clouds play a crucial role in the Earth system. The radiative properties of clouds have a large influence on climate, and precipitation from clouds affects all land-dwelling life on Earth, including human beings. Many numerical cloud models have been developed to investigate and predict such effects. These can be divided into two groups according to their microphysical representation: bulk and spectral bin models. Bulk models are widely used in cloud-resolving models, including both general circulation models and mesoscale models. In bulk models, all microphysical processes are described in terms of averaged parameters, such as mixing ratios or number concentrations of cloud hydrometeors, such as liquid cloud, rain, cloud ice, snow, and graupel. One-moment models prognose only the mass mixing ratios of these categories, while two-moment models also prognose number concentrations. Many attempts have been made to improve bulk models, for example by increasing the number of categories (e.g., Straka and Mansell 2005) and moments (e.g., Milbrandt and Yau 2005a,b) that are prognosed. In bulk models, the parameters of the hydrometeor spectra are diagnosed from averaged quantities. In contrast, in spectral bin models the size or mass distributions of the hydrometeors are modeled directly. Instead of being prescribed a priori, as in bulk models, the shapes of the size distributions are explicitly calculated following physical laws.

Because of the rapid progress of supercomputers, it is now feasible to use bin models for mesoscale clouds (e.g., Lynn et al. 2005; Khain and Lynn 2009), but there are still large limitations on their use because of the large computational costs. Many bin models now include ice-phase processes (Khain et al. 2004; Rasmussen et al. 2002; Reisin et al. 1996), incurring still greater costs. For example, the Hebrew University Cloud Model (HUCM; Khain et al. 2004) has six categories for solid water. When calculating coagulations of particles using n_{bin} classes for liquid water and six categories of solid water, the number of combinations to be dealt with is ${}_7C_2 n_{\mathrm{bin}}^2$, which is 21 times more costly than for liquid water alone. Sato et al.

* Supplemental information related to this paper is available at the Journals Online website: http://dx.doi.org/10.1175/JAS-D-11-0166.s1.

Corresponding author address: Ryo Onishi, Earth Simulator Center, Japan Agency for Marine–Earth Science and Technology, 3173-25 Showa-machi, Kanazawa-ku, Yokohama, Kanagawa 236-0001, Japan. E-mail: onishi.ryo@jamstec.go.jp

DOI: 10.1175/JAS-D-11-0166.1

(2009) proposed a Monte Carlo method to decrease these costs by randomly selecting the combinations to be dealt with, but this raises questions about the best compromise between cost and reliability. Bin models that include solid water, such as the HUCM and the models of Reisin et al. (1996) and Rasmussen et al. (2002), are sometimes called full-bin models, but it is doubtful whether the spectral treatment of solid water improves the reliability. For example, Li et al. (2010) had to tune the HUCM using observational data, which clearly shows that there are uncertainties even in the full-bin models. Moreover, it is probably not sufficient to divide solid water into just six categories; ideally, we would like to deal with additional dimensions such as density or shape. In this sense, a ''real'' full-bin model would require a much larger number of categories.

Recently, Shima et al. (2009) developed the super-droplet model (SDM), based on a Lagrangian approach rather than the conventional Eulerian method. In cases where there are five or more dimensions for cloud substance, the SDM has an advantage in terms of computational cost. In models that consider three dimensions for space (x, y, and z), and one each for size and density or shape (for solid water)—that is, five in total—it might therefore be better to use the SDM approach rather than bin models. If further dimensions are used for CCN compositions, the advantage of the SDM approach increases further. However, the SDM is still under development and cannot immediately be used for major applications.

In this study, we propose a simple way of making bin models developed for warm clouds applicable to cold clouds by using a bin–bulk hybrid approach. In this method, a spectral bin scheme is used for liquid droplets, while a bulk scheme is used to treat the solid particles. In the bulk part, the prognostic variables are the mixing ratios of cloud ice, snow, and graupel and the number densities of cloud ice particles. The basic idea is very simple; the expensive but more reliable spectral bin scheme treats the relatively well-understood physics of the liquid phase, and the computationally efficient but less robust bulk scheme is used to treat the poorly understood physics of the ice phase. Thus, the hybrid approach combines two good features: reliability for warm-rain simulations and applicability to cold rain. The bin–bulk hybrid model has been implemented into the Multi-Scale Simulator for the Geoenvironment (MSSG; Takahashi et al. 2005) developed in the Earth Simulator Center of the Japan Agency for Marine–Earth Science of Technology (JAMSTEC). Thus, we have named our model MSSG-Bin. MSSG (usually pronounced ''message'') also includes a conventional one-moment bulk model named MSSG-Bulk. In this paper, we perform intercomparisons among one-moment bulk models, two-moment bulk models, and spectral bin models to confirm the anticipated features of MSSG-Bin.

It should be noted that there are several so-called hybrid approaches combining bin and bulk schemes. Farley and Orville (1986) proposed a hybrid model where a bin treatment is adopted for precipitating ice categories, and a bulk treatment for cloud ice and liquid water categories. That is, it can be considered a (partial) ice-bin–warm-bulk hybrid model. Feingold et al. (1998) proposed a hybrid model in which the mixing ratio and number concentrations from a two-moment bulk-parameterization model are converted to bins with prescribed size distributions, and computations are then performed with a bin model. Results are then converted back to the bulk microphysical model. This hybrid approach gives a better representation of droplet growth within each time step, without the large data storage required by a bin model. However, an important limitation of this approach is that it does not produce the same results as a pure bin treatment because the bin parameterization solution is not carried from time step to time step; that is, some information is lost when converting back and forth between the bulk and bin parameterizations (Straka 2009). For example, the representation of hydrometeor sedimentation follows the bulk parameterization, which does not represent well the basic physical fact that larger drops sediment faster. In contrast, the hybrid approach proposed here acts as a pure bin model for warm clouds.

In the following section, we describe the details of our bin–bulk hybrid cloud microphysical model. Results and discussion for one-dimensional and three-dimensional model intercomparisons are presented in sections 3 and 4, respectively. After describing the computational performance of our code in section 4d, the study is concluded in section 5.

2. Model description

a. Dynamics

The MSSG is an atmosphere–ocean coupled model aimed at seamless simulations from global to local scales (Takahashi et al. 2005). MSSG adopts the conventional latitude–longitude (lat-lon) grid system for regional simulations, and the yin–yang grid (Kageyama and Sato 2004)—consisting of two overlapping lat-lon grids—for global simulations, thus avoiding the grid convergence problem at the poles. Here we summarize the atmospheric component (MSSG-A). The dynamical core of MSSG-A is based on the nonhydrostatic equations and predicts the three wind components and air density and pressure (Takahashi et al. 2005; Baba et al. 2010). The third-order Runge–Kutta scheme is used for time

integrations, and the fast terms relating to acoustic and gravity waves are calculated separately with shorter time steps (Wicker and Skamarock 2002). A fifth-order upwind scheme (Wicker and Skamarock 2002) is usually chosen for advection, and for turbulent diffusion either the Mellor–Yamada–Nakanishi–Niino (Nakanishi and Niino 2009) or static Smagorinsky model is used, depending on the resolution.

b. Governing equations for cloud microphysics

The MSSG-Bin model employs a spectral bin scheme for liquid water and a conventional bulk scheme for solid water. The bulk component prognoses mixing ratios of cloud ice Q_i, snow Q_s, and graupel Q_g, and the number density of cloud ice particles N_i. There are additional options available to prognose the number concentrations of snow N_s and graupel N_g particles. However, this study only discusses the default setting, where only N_i is prognosed.

The spectral bin scheme prognoses the mass distribution function $g(y, t)$, where $y = \ln r$ (natural logarithm of the droplet radius); $g(y, t)$ is given by

$$g(y,t)\,dy = n_p(r,t)m(r)\,dr, \tag{1}$$

where n_p is the number density function. The mass coordinate m and logarithmic coordinate y are discretized as

$$m_k = 2^{1/s} m_{k-1}, \tag{2}$$

$$y_k = y_{k-1} + dy, \tag{3}$$

where $dy = \ln 2/(3s)$, with s being a constant. Note that $s = 1$ leads to a mass-doubling resolution, which is the default value for MSSG-Bin. The representative radius of the first bin, r_1 ($=e^{y1}$), is set to 3 μm. In the default configuration, 33 classes are calculated, resulting in a largest drop class with representative radius $r_{33} = 4.9$ mm. The representative mass distribution function of class k, ξ_k, is defined through the mass content M_k as

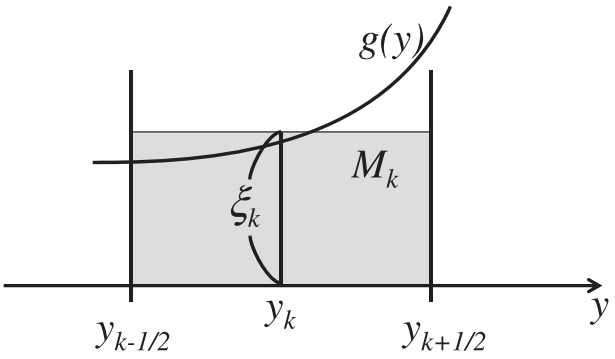

FIG. 1. Discretization in the MSSG-Bin model.

$$M_k = \int_{y_{k-1/2}}^{y_{k+1/2}} g(y)\,dy \equiv \xi_k\,dy, \tag{4}$$

where $y_{k\pm1/2} = y_k \pm dy/2$ are the boundaries of the class (see Fig. 1). The number content in class k is then calculated as

$$N_k = \int_{y_{k-1/2}}^{y_{k+1/2}} \frac{\xi_k}{m}\,dy = \frac{\xi_k(2^{1/2s} - 2^{-1/2s})}{3m_k}, \tag{5}$$

leading to a mean droplet mass in class k of $\overline{m_k} = M_k/N_k = m_k \ln 2/[s(2^{1/2s} - 2^{-1/2s})]$. The total mass of liquid water $\rho_d Q_w$, where ρ_d and Q_w are the dry air mass and the mixing ratio of total liquid water, is obtained from

$$\rho_d Q_w = \sum_{k=1}^{n_{\text{bin}}} M_k, \tag{6}$$

where n_{bin} is the number of bins. Prognostic variables are the mixing ratios of water vapor Q_v, liquid droplet M_k ($=\xi k\,dy$), cloud ice, snow, and graupel, as well as the number concentrations of dry cloud condensation nuclei (CCN) N_{ccn} and cloud ice particles. The governing equations for the prognostic variables are written as

$$\frac{\partial \rho_d Q_v}{\partial t} = -\text{ADV}(\rho_d Q_v) + \text{DIV}(\rho_d Q_v) + \text{DIFF}(\rho_d Q_v) - \sum_k \left(\frac{\partial M_k}{\partial t}\right)_{\text{cond}} + \rho_d(-P_{\text{idsn}} - P_{\text{idep}} - P_{\text{sdep}} - P_{\text{gdep}}), \tag{7}$$

$$\frac{\partial M_k}{\partial t} = -\text{ADV}(M_k) + \text{DIV}(M_k) + \text{DIFF}(M_k) + \left(\frac{\partial M_k}{\partial t}\right)_{\text{nucl}} + \left(\frac{\partial M_k}{\partial t}\right)_{\text{coad}} + \left(\frac{\partial M_k}{\partial t}\right)_{\text{coag}} + \left(\frac{\partial M_k}{\partial t}\right)_{\text{breakup}} + \left(\frac{\partial M_k}{\partial t}\right)_{\text{hybrid}} - U_k \frac{\partial M_k}{\partial x_3}, \tag{8}$$

$$\frac{\partial N_{\text{ccn}}}{\partial t} = -\text{ADV}(N_{\text{ccn}}) + \text{DIV}(N_{\text{ccn}}) + \text{DIFF}(N_{\text{ccn}}) - \left(\frac{\partial N_{\text{ccn}}}{\partial t}\right)_{\text{nucl}} + \left(\frac{\partial N_{\text{ccn}}}{\partial t}\right)_{\text{recycle}}, \tag{9}$$

$$\frac{\partial \rho_d Q_i}{\partial t} = -\mathrm{ADV}(\rho_d Q_i) + \mathrm{DIV}(\rho_d Q_i) + \mathrm{DIFF}(\rho_d Q_i) + \rho_d(P_{\mathrm{idsn}} + P_{\mathrm{ifzc}} + P_{\mathrm{ispl}} + P_{\mathrm{idep}} + P_{\mathrm{i,iacw}} - P_{\mathrm{icng}} - P_{\mathrm{raci}} - P_{\mathrm{saci}} - P_{\mathrm{icns}} - P_{\mathrm{imlt}}), \quad (10)$$

$$\frac{\partial \rho_d Q_s}{\partial t} = -\mathrm{ADV}(\rho_d Q_s) + \mathrm{DIV}(\rho_d Q_s) + \mathrm{DIFF}(\rho_d Q_s) + \rho_d(P_{\mathrm{sdep}} + P_{\mathrm{icns}} + P_{\mathrm{s,sacw}} - P_{\mathrm{scng}} + P_{\mathrm{saci}} + P_{\mathrm{s,sacr}} - P_{\mathrm{g.racs}} - P_{\mathrm{smlt}}) - U_s \frac{\partial \rho_d Q_s}{\partial x_3}, \quad (11)$$

$$\frac{\partial \rho_d Q_g}{\partial t} = -\mathrm{ADV}(\rho_d Q_g) + \mathrm{DIV}(\rho_d Q_g) + \mathrm{DIFF}(\rho_d Q_g) + \rho_d(P_{\mathrm{gdep}} + P_{\mathrm{scng}} + P_{\mathrm{g.sacw}} + P_{\mathrm{gacw}} + P_{\mathrm{gacr}} + P_{\mathrm{iacr}} + P_{\mathrm{raci}} + P_{\mathrm{g.sacr}} + P_{\mathrm{gfzr}} + P_{\mathrm{icng}} + P_{\mathrm{g.iacw}} - P_{\mathrm{gmlt}}) - U_g \frac{\partial \rho_d Q_g}{\partial x_3}, \quad (12)$$

$$\frac{\partial N_i}{\partial t} = -\mathrm{ADV}(N_i) + \mathrm{DIV}(N_i) + \mathrm{DIFF}(N_i) + \rho_d \left[-N_{\mathrm{icng}} - N_{\mathrm{iag}} + \frac{1}{m_i}(P_{\mathrm{idsn}} + P_{\mathrm{ispl}} + P_{\mathrm{ifzc}}) - \frac{N_i}{Q_i}(P_{\mathrm{imlt}} + P_{\mathrm{raci}} + P_{\mathrm{saci}} + P_{\mathrm{icns}}) \right], \quad (13)$$

where the ADV, DIV, and DIFF terms represent three-dimensional advection, divergence, and diffusion, and U_x is the sedimenting velocity of species x. The liquid drop terminal velocities U_k are obtained following Beard (1976). The ADV terms and gravitational sedimentation terms are calculated using the second-order weighted average flux (WAF) method using the Superbee flux-limiter (Toro 1989), which is a total variation diminishing (TVD)-type scheme.

c. Warm-rain part (spectral bin calculation)

1) CCN ACTIVATION AND RECYCLING

The formulation of the drop activation process is based on the relationship between the number of activated CCN N_{act} and the saturation ratio with respect to water S_w (Twomey 1959; Khairoutdinov and Kogan 2000). In Twomey (1959), the relationship between N_{act} and S_w takes the form $N_{\mathrm{act}} = CS_w^k$, where C and k are suitable parameters based on the class of CCN (the so-called Twomey relationship). If we define S_{max} as the supersaturation needed to activate the total particle count $N_{\mathrm{ccn}} + N_w$, where N_{ccn} and $N_w(=\sum N_k)$ are the number concentrations of dry CCN and liquid droplets, then C can be represented as $C = (N_{\mathrm{ccn}} + N_w)S_{\mathrm{max}}^{-k}$. Thus, the number of activated CCN can be expressed as follows:

$$N_{\mathrm{act}} = (N_{\mathrm{ccn}} + N_w)\left(\frac{S_w}{S_{\mathrm{max}}}\right)^k. \quad (14)$$

The number of newly nucleated droplets is calculated as

$$N_{\mathrm{nucl}} = \max\{0, (N_{\mathrm{ccn}} + N_w)\min[1, (S_w/S_{\mathrm{max}})^k] - N_w\}, \quad (15)$$

leading to $(\partial N_{\mathrm{ccn}}/\partial t)_{\mathrm{nucl}} = N_{\mathrm{nucl}}/\Delta t$. MSSG-Bin has two options for the CCN activation process, one for maritime and one for continental conditions. The parameters k and S_{max} are set at 0.6 and 1.008 in the maritime case, and 0.4 and 1.0048 in the continental case. These values are within the observed ranges reported within the literature (e.g., Soong 1974; Pruppacher and Klett 1997; Khairoutdinov and Kogan 2000; Lim and Hong 2010).

It should be noted that there are two classes of CCN activation scheme based on the Twomey relationship. One class prognoses either the number of activated CCN or the maximum supersaturation S_{max} experienced by the air parcel during the activation process (Stevens et al. 1996; Rasmussen et al. 2002; Grabowski et al. 2011). The other class prognoses the total number of CCN (Khairoutdinov and Kogan 2000; Lim and Hong 2010). This study chooses the latter, but in the sense that one CCN particle is consumed when one CCN is activated and forms a water droplet, each class deals with the same information.

Representation of the Twomey relationship typically involves adding activated droplets to the first bin. However, Grabowski and Wang (2008) report that such an approach fails to converge as the number of bins increases. A sensible modification is to insert activated droplets into the bins corresponding to their activation radii. One problem of this modification is that it requires bin sizes below 1 μm (Grabowski et al. 2011); otherwise, most of the activated droplets end up in the first radius

bin. MSSG-Bin currently employs a simpler method; the ''prescribed-spectrum'' method (Soong 1974; Reisin et al. 1996), which is insensitive to the size of the smallest bin and more robust in terms of convergence. In Soong (1974), the size distribution of activated CCN is prescribed in an exponential form:

$$n_r(r) = N_{\text{nucl}}\left(\frac{3r^2}{\bar{r}^3}\right)\exp\left[-\left(\frac{r}{\bar{r}}\right)^3\right], \qquad (16)$$

where $\bar{r}$ is the mean radius of the activated CCN and is set to 11.0 μm in the maritime case and 5.0 μm in the continental case. The mean mass of activated CCN is $\overline{m} = 4\pi\rho_w\bar{r}^3/3$. The number of newly nucleated droplets is limited so that $\overline{m}N_{\text{nucl}} \leqq \rho_d Q_{v,\text{sat}} \max(0, S_w - 1)$, where $Q_{v,\text{sat}}$ is the saturated mixing ratio for water vapor with respect to water. This method does not allow a detailed treatment of, for example, activation radii or the solute characteristics of aerosols. However, it does allow us to represent the difference between maritime and continental aerosols. Moreover, it also has the advantage that the activation process of giant CCN can be implemented easily in the same manner.

The observational data indicate that $5 \times 10^7 < N_{\text{ccn}} < 2.5 \times 10^8$ m^{-3} for maritime conditions, and $6 \times 10^8 < N_{\text{ccn}} < 5 \times 10^9$ m^{-3} for continental conditions (Pruppacher and Klett 1997). MSSG-Bin sets the initial dry CCN concentrations to $N_{\text{ccn}} = \rho_d n_{\text{ccn}}$, where $n_{\text{ccn}} = 7 \times 10^7$ for maritime and $n_{\text{ccn}} = 1 \times 10^9$ for continental conditions.

Evaporated liquid droplets leave behind dry CCN. Droplets that become smaller than $y_{1/2}$ are considered as evaporated and thus are added to the number of dry CCN.

2) Condensation/evaporation of liquid droplets

The diffusional growth rate of liquid mass is calculated as

$$\left(\frac{dm}{dt}\right)_{\text{cond/evap}} = C_w[P(t), T(t)]\Delta S_w m^{1/3}, \qquad (17)$$

where ΔS_w is the supersaturation ratio defined as $\Delta S_w = (Q_v - Q_{v,\text{sat}})/Q_{v,\text{sat}}$. The term C_w is a function of pressure and temperature (Tzivion et al. 1989).

We adopt an inner time loop for the diffusional growth calculation. The number of inner loop time steps n_d is set just large enough that the time step length Δt_d is less than a given limit Δt_{d0}; that is, $n_d = \text{INT}(\Delta t/\Delta t_{d0}) + 1$, leading to a time step length $\Delta t_d = \Delta t/n_d$. On the nth step of the inner time loop, the change of the droplet mass is calculated as $\int_{t+(n-1)\Delta t_d}^{t+n\Delta t_d} C_w S_w m^{1/3}\, d\tau$, using the analytical solution that can be found in, for example, appendix B in Tzivion et al. (1989). To calculate new values of the distribution functions, the new spectrum has to be remapped to conform to the new mass. We adopt a simple remapping scheme (Kovetz and Olund 1969; Khain et al. 2004): for the case $m_i \leqq m_k^{t+\Delta t} < m_{i+1}$, we set $(\Delta M_i)^t = c\Delta M_k^t$ and $(\Delta M_{i+1})^t = (1-c)\Delta M_k^t$, where $c = (m_k^{t+\Delta t} - m_i)/(m_{i+1} - m_i)$. This remapping usually leads to the artificial formation of larger droplets. One effective remedy is to increase the size resolution (i.e., to increase s). This is the method used in this study, and later we demonstrate its convergence with increasing s. Another remedy is to prognose the number concentration as well (i.e., to use a two-moment method). This will be tested in future work.

3) Coagulation of liquid droplets

The coagulation growth of droplets is modeled by the stochastic collision–coalescence equation (SCE). The coagulation kernel K_{coag} is equal to the product $E_{\text{coal}}E_cK_c$, where E_{coal}, E_c, and K_c are the coalescence efficiency, collision efficiency, and collision kernel, respectively. The table in Hall (1980) is used for E_c. For coalescence efficiencies MSSG-Bin adopts the formulation of Low and List (1982a) for collision pairs between 50 μm $< r_s$ and 50 μm $< r_l$, and that of Beard and Ochs (1984) for $30 < r_s < 50$ μm and 50 μm $< r_l$, where r_s and r_l are the radii of the smaller and larger of the two drops. Outside these ranges we set the coalescence efficiency to 0.6 (Beard and Ochs 1995). The exponential flux method (EFM) (Bott 2000) is used to solve the discretized SCE.

4) Breakup of liquid droplets

Fragmentation of large drops may be induced by the collision of drops with each other (''collisional breakup'') or by hydrodynamic instabilities of the drops (''spontaneous breakup''). Observations show, however, that drops large enough to enter the realm of spontaneous breakup (diameter > 5 mm) are very rare in atmospheric clouds. Indeed, the model calculations of Young (1975), where both breakup modes were included, show that spontaneous breakup is negligible. Furthermore, the spectral shape produced by a balance between spontaneous breakup and coalescence is unrealistically flat (i.e., there is too great a bias toward larger drop sizes) (Srivastava 1971; Tsias 1996). Therefore, MSSG-Bin considers only collisional breakup. This is described by the stochastic breakup equation (SBE). The SBE requires a collisional breakup kernel $K_b(i,j) = [1 - E_{\text{coal}}(i,j)]E_c(i,j)K_c(i,j)$, which describes the collision of a mass m_i drop with a mass m_j drop. The fragment size distribution $Q(k; i, j)$ specifies the mean number of fragments of mass m_k per collision and subsequent breakup of the

two drops. The fragment size distributions are parameterized following Low and List (1982b), but with some corrections for small raindrops using parameterizations given by Beard and Ochs (1995).

d. Ice-phase microphysics

Figure 2 shows the cloud microphysical processes considered in MSSG-Bin and MSSG-Bulk. (Refer to the tables in the appendix for a description of each process.) The ice-phase microphysics of MSSG-Bin is taken directly from MSSG-Bulk, which is based on Reisner et al. (1998) with some modifications by Thompson et al. (2004). The prognostic variables are the mixing ratios of water vapor, cloud, rain, cloud ice, snow, and graupel, and the number concentrations of cloud ice, snow (optional), and graupel (optional); Q_v, Q_c, Q_r, Q_i, Q_s, Q_g, N_i, N_s, and N_g. In this study, the optional variables N_s and N_g are not used.

The size distribution functions for snow and graupel are expressed via inverse exponential relationships of the form

$$dN_x(D_x) = N_{0x}\exp(-\lambda_x D_x)\,dD_x \quad \text{for} \quad x = s \text{ or } g, \tag{18}$$

where λ_x [equal to $(\pi\rho_x N_x/\rho_d Q_x)^{1/3}$, where ρ_x and N_x are the density and total number density of species x] is the slope parameter, and N_{0x} [equal to $N_x(\pi\rho_x N_x/\rho_d Q_x)^{1/3}$] is the intercept parameter. In two-moment schemes, where both Q_x and N_x are prognosed, both the slope and intercept parameters can be determined directly. However, schemes such as MSSG-Bulk and MSSG-Bin, which adopt one-moment schemes for snow and graupel, need an empirical parameterization to determine the two parameters. The intercept parameter for graupel N_{0g} is set to 4×10^6. For snow, the intercept parameter is given by $N_{0s} = \min\{2 \times 10^8, 2 \times 10^8 \exp[-0.12 \min(-0.001, T - T_{\text{frz}})]\}$, where T_{frz} is the freezing temperature (Thompson et al. 2004). As for the cloud ice, the mean state is considered instead of the full size distribution. The mean diameter $\overline{D_i}$ is diagnosed as $\overline{D_i} = (6\rho_d Q_i/\pi\rho_i N_i)^{1/3}$, where ρ_i is the density of cloud ice. Note that MSSG-Bulk and MSSG-Bin prognose both N_i and Q_i. The sedimenting velocities of snow and graupel are assumed to take a power-law form; $U_x(D_x) = a_x D_x^{b_x}(\rho_0/\rho_a)^{1/2}$, where $\rho_0 = 1.18$ kg m^{-3} is a reference density and ρ_a the air density. The mass-weighted mean sedimenting velocities are then given by $U_x = a_x\Gamma(4 + b_x)/6\lambda_x^{b_x}$. The parameters a_x and b_x are as suggested in Reisner et al. (1998).

e. Hybrid processes

In the hybrid scheme, we need to provide an interface (hereafter referred to as the "hybrid interface") between the bulk and spectral bin quantities. This study proposes two such interfaces, a size-independent interface (SII) and a size-dependent interface (SDI).

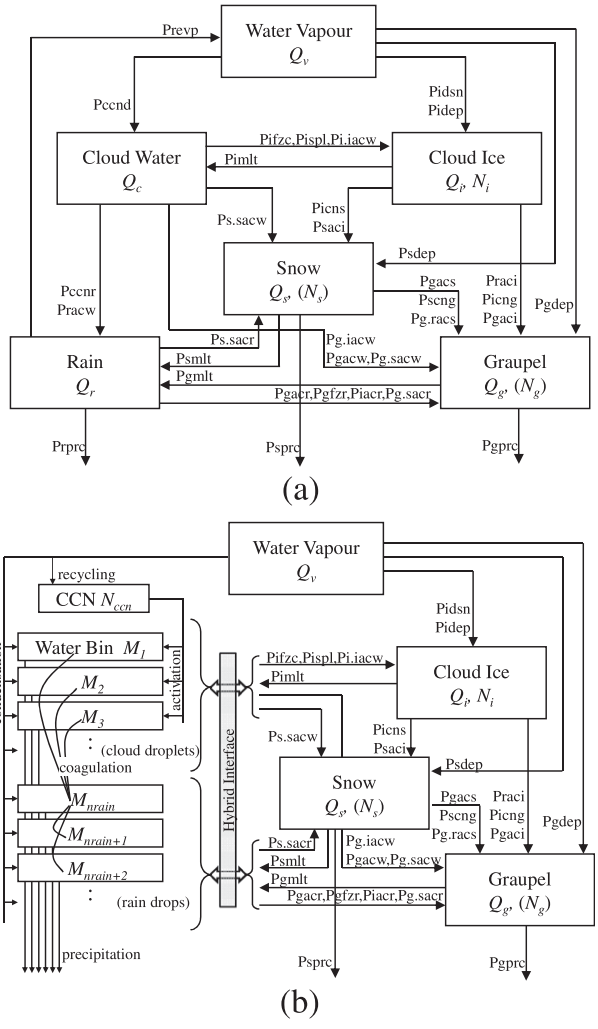

FIG. 2. Cloud microphysical processes in (a) MSSG-Bulk and (b) MSSG-Bin.

1) SIZE-INDEPENDENT INTERFACE

In the SII, the bulk cloud and rain mixing ratios are calculated from the spectral bin quantities as

$$\rho_d Q_c = \sum_{k=1}^{n_{\text{cloud}}} M_k \quad \text{and} \quad \rho_d Q_r = \sum_{k=n_{\text{cloud}}+1}^{n_{\text{bin}}} M_k, \tag{19}$$

where n_{cloud} is the number of classes for which r_k is less than or equal to a given cutoff value r_{cutoff}, which we default to 40 μm. The ice-phase processes change the bulk liquid mixing ratios Q_c and Q_r through freezing, melting, and collection:

$$\left(\frac{\partial \rho_d Q_c}{\partial t}\right)_{i,s,g} = \rho_d(-P_{\text{ifzc}} - P_{\text{ispl}} - P_{\text{s.sacw}} - P_{\text{g.sacw}} - P_{\text{gacw}} - P_{\text{i.iacw}} - P_{\text{g.iacw}} + P_{\text{imlt}}) \tag{20}$$

and

$$\left(\frac{\partial \rho_d Q_r}{\partial t}\right)_{i,s,g} = \rho_d(-P_{\text{gfzr}} - P_{\text{iacr}} - P_{\text{s.sacr}} - P_{\text{g.sacr}} - P_{\text{gacr}} + P_{\text{smlt}} + P_{\text{gmlt}}), \tag{21}$$

where the RHS terms are as described in appendix A. Conversely, the changes in bulk quantities are used to update the spectral bin quantities. Here we assume that the liquid mixing ratio in each spectral bin is multiplied by the same factor, which depends on the changes in bulk quantities as

$$\left(\frac{\partial M_k}{\partial t}\right)_{\text{hybrid}} = \begin{cases} \left(\frac{\partial \rho_d Q_c}{\partial t}\right)_{i,s,g} \Big/ (\rho_d Q_c) \times M_k & \text{for} \quad k \leqq n_{\text{cloud}} \\ \left(\frac{\partial \rho_d Q_r}{\partial t}\right)_{i,s,g} \Big/ (\rho_d Q_r) \times M_k & \text{for} \quad k > n_{\text{cloud}} \end{cases}. \tag{22}$$

2) SIZE-DEPENDENT INTERFACE

In the SDI, we consider the size-dependence of the temporal changes of mass due to ice-phase processes. The hybrid-process term is written as

$$\left(\frac{\partial M_k}{\partial t}\right)_{\text{hybrid}} = -\left(\frac{dM_k}{dt}\right)_{\text{frz}} + \left(\frac{dM_k}{dt}\right)_{\text{imlt}} + \left(\frac{dM_k}{dt}\right)_{\text{smlt}} + \left(\frac{dM_k}{dt}\right)_{\text{gmlt}} - \left(\frac{dM_k}{dt}\right)_{\text{iac}\underline{k}} - \left(\frac{dM_k}{dt}\right)_{\text{sac}\underline{k}} - \left(\frac{dM_k}{dt}\right)_{\text{gac}\underline{k}}, \tag{23}$$

where the subscript frz denotes freezing of water, *x*mlt melting of ice species *x* (i = cloud ice, s = snow, and g = graupel), and *x*ac$\underline{k}$ the collection of liquid water in class $\underline{k}$ by ice species *x*.

Freezing is treated as in Bigg (1953). Frozen droplets ($r_k \leq r_{\text{cutoff}}$) become cloud ice, and frozen drops ($r_k \geq r_{\text{cutoff}}$) become graupel. The mass of the melted ice particles is inserted into bins according to the mean masses $\overline{m}_i, \overline{m}_s$, and $\overline{m}_g$. The collection of liquid water by cloud ice is dependent on the size of the droplets/drops and the mean diameter of cloud ice $\overline{D}_i$, while that of snow and graupel depends on the exponential size distributions of snow and graupel (see section 2d). The equation for each term is given in appendix C.

3. 1D intercomparison experiments

a. Intercomparison framework

One-dimensional experiments were carried out within the ''Kinematic Driver'' (KiD) intercomparison framework developed at the UK Met Office (Shipway and Hill 2011; http://appconv.metoffice.com/microphysics/). KiD is designed as a basic wrapper for consistent testing of different microphysical models using a common advection component, and it provides a consistent and flexible framework for forcing microphysical models. The exclusion of complex feedbacks between microphysics and dynamics leads to a more straightforward comparison between models.

At the time of writing, the following model codes were available from the above Web site: the Land Evaluation Model, version 2.4 (LEM2.4; Abel and Shipway 2007), the Weather Research and Forecasting (WRF) Single-Moment Six-Class Microphysics Scheme (WSM6; Hong and Lim 2006), Thompson (two-moment version; Thompson et al. 2008), hereafter referred to as Thompson(2M), Morrison (Morrison et al. 2005; Morrison and Pinto 2005), the WRF Double-Moment Six-Class Microphysics Scheme (WDM6; Lim and Hong 2010), and the Tel-Aviv University bin model (TAU-Bin; Tzivion et al. 1987; Feingold et al. 1988; Tzivion et al. 1989). The Web site also provides results for Thompson (one-moment version; Thompson et al. 2004, 2008)—hereafter referred to as Thompson(1M)—which we also include in our intercomparisons. However, because the model code was not available from the Web site, we have not included it in the comparisons of computational performance in Tables 1 and 2.

b. Shallow convection case (warm rain)

Case 1 in KiD uses a simple updraft, which is sinusoidal in time and constant in height, to advect vapor and hydrometeors. The temperature field is kept fixed so as to minimize feedback from the different microphysical models. The updraft is externally given as

$$w(z,t) = \begin{cases} w_1 \sin(\pi t/600) & \text{for} \quad t < 600\,\text{s} \\ 0.0 & \text{otherwise} \end{cases}, \tag{24}$$

where w_1 is set to 2 m s^{-1}. The initial profiles of temperature and moisture are set to be similar to those used in the Global Energy and Water Cycle Experiment (GEWEX) Cloud System Study (GCSS) Rain in Cumulus over the Ocean (RICO) composite intercomparison (see also section 4a). The duration and depth of the simulation

TABLE 1. Prognostic variables and floating-point operation (FPO) ratio with respect to MSSG-Bulk for the shallow convective cloud case in KiD (N/A stands for not available).

	Model name	Prognostic variables	FPO ratio
One-moment	MSSG-Bulk	Q_v, Q_c, Q_r	1.00
	Thompson(1M)	Q_v, Q_c, Q_r	N/A
	WSM6	Q_v, Q_c, Q_r	1.16
Two-moment	Thompson(2M)	Q_v, Q_c, Q_r, N_r	1.37
	Morrison	Q_v, Q_c, Q_r, N_r	1.30
	WDM6	Q_v, Q_c, Q_r, N_{ccn}, N_c, N_r	1.48
Bin	TAU-Bin	Q_v, $\xi_k(34)$, $N_k(34)$, N_{ccn}	29.0
	MSSG-Bin(s1)	Q_v, $\xi_k(33)$, N_{ccn}	8.30
	MSSG-Bin(s2)	Q_v, $\xi_k(66)$, N_{ccn}	19.2
	MSSG-Bin(s4)	Q_v, $\xi_k(132)$, N_{ccn}	50.7
	MSSG-Bin(s8)	Q_v, $\xi_k(264)$, N_{ccn}	154
	MSSG-Bin(s16)	Q_v, $\xi_k(528)$, N_{ccn}	525

are 3600 s and 3000 m, respectively. All the KiD simulations reported here used a time step length dt of 1 s.

Table 1 provides descriptions of the models that have been compared for this case. We classify the models into three groups; one-moment bulk (1-BULK) models, two-moment bulk (2-BULK) models, and spectral bin (BIN) models. In this study, we consider a bulk model as a two-moment model if the model prognoses the number concentration of rain droplets. As an index of computational cost, the table also reports the floating-point operation (FPO) ratio compared with MSSG-Bulk. Two spectral bin models are shown: TAU-Bin and MSSG-Bin, with the latter using several different values of s. Hereafter, the MSSG-Bin simulation with $s = X$ is referred to as MSSG-Bin(sX). None of the bin simulations for shallow clouds considered collisional breakup, since such breakup does not play a significant role in shallow clouds.

The 2-BULK models require several tens of percent more FPOs than the 1-BULK models, and the BIN models orders of magnitude more. MSSG-Bin(s1) requires fewer FPOs than TAU-Bin because there are only around half the number of prognostic variables. MSSG-Bin with $s = 2$—i.e., MSSG-Bin(s2)—requires a similar number of FPOs to TAU-Bin, and MSSG-Bin(s4) somewhat more. We see that the number of FPOs becomes roughly proportional to s^2 for large s. The logarithms to base 2 of the FPO ratio between MSSG-Bin(s2X) and MSSG-Bin(sX)—denoted $\ln_2$ [FPO(s2X)/FPO(sX)]—are 1.20, 1.41, 1.61, and 1.77 for $s = 1$, 2, 4, and 8. This quadratic dependence on large s is attributable to the coagulation calculation, which needs to check each individual pair of bins. In contrast, the condensation calculation, requiring FPOs proportional to s, dominates the required FPOs for small s.

Figure 3 shows the liquid water path (LWP) and rainwater path (RWP) for the (a) 1-BULK, (b) 2-BULK, and (c) BIN models. While the updraft is maintained ($t < 600$ s), LWP increases with time. When the updraft is turned off, the LWP starts to decrease due to precipitation and the evaporation of falling rain. More precisely, the decrease of LWP starts when RWP reaches its maximum, suggesting that the evaporation of falling rain initiates the decrease of LWP. A notable difference between the three model categories is the shape of the curves around $t = 600$ s. As the updraft ends, the LWP of the 1-BULK models decrease sharply, while those of the 2-BULK models have a short buffer period. The results of the BIN models have an even longer buffer period. The sharp decrease in the 1-BULK models is attributable to their overestimate of the conversion

TABLE 2. Prognostic variables and floating-point operation (FPO) ratio with respect to MSSG-Bulk for the deep convective cloud case in KiD.

	Model name	Prognostic variables	FPO ratio
One-moment	MSSG-Bulk	Q_v, Q_c, Q_r, Q_i, Q_s, Q_g, N_i	1.00
	Thompson(1M)	Q_v, Q_c, Q_r, Q_i, Q_s, Q_g, N_i	N/A
	WSM6	Q_v, Q_c, Q_r, Q_i, Q_s, Q_g, N_i	0.91
Two-moment	Thompson(2M)	Q_v, Q_c, Q_r, Q_i, Q_s, Q_g, N_r, N_i	1.19
	Morrison	Q_v, Q_c, Q_r, Q_i, Q_s, Q_g, N_r, N_i, N_s, N_g	1.25
	WDM6	Q_v, Q_c, Q_r, Q_i, Q_s, Q_g, N_{ccn}, N_c, N_r	1.10
Bin	MSSG-Bin[SDI]	Q_v, $\xi_k(33)$, Q_i, Q_s, Q_g, N_{ccn}, N_i	9.04
	MSSG-Bin[SDI](s4)	Q_v, $\xi_k(132)$, Q_i, Q_s, Q_g, N_{ccn}, N_i	53.4
	MSSG-Bin[SII](s4)	Q_v, $\xi_k(132)$, Q_i, Q_s, Q_g, N_{ccn}, N_i	56.5

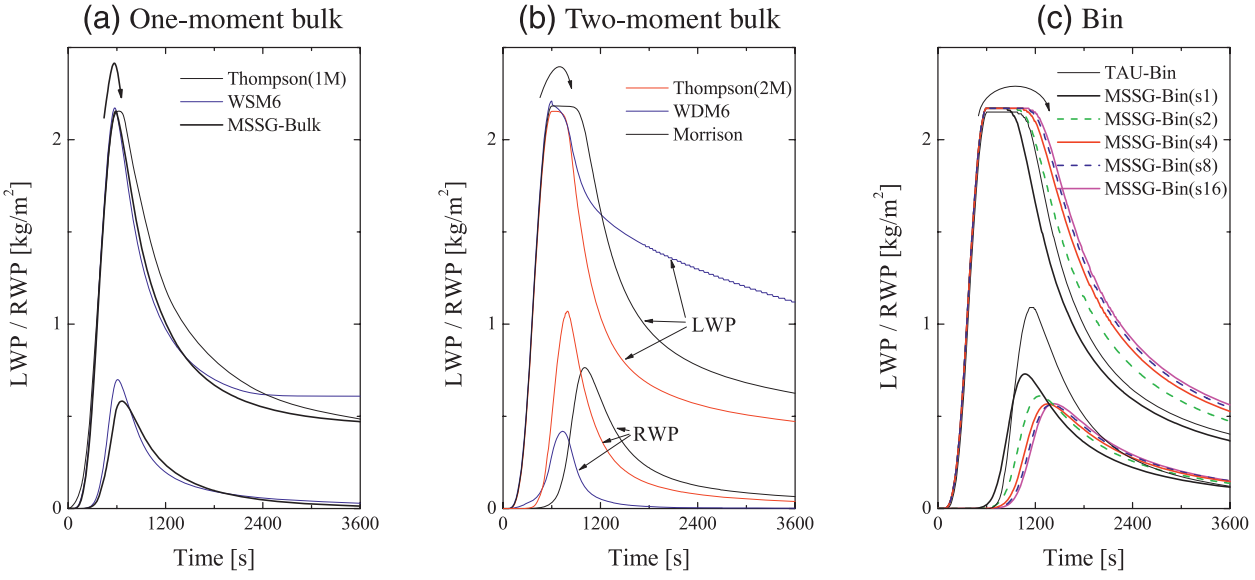

FIG. 3. Liquid water path (LWP) and rainwater path (RWP) for the KiD shallow convective cloud case.

rate from cloud to rain (often referred to as the autoconversion rate). As confirmed by the subsequent figures, this overestimate leads to larger amounts of rain, which then evaporates as it falls. MSSG-Bin shows longer buffer periods after $t = 600$ s for larger values of s. The MSSG-Bin results converge for $s \geq 4$. As mentioned above, the simulations used a time step length dt of 1 s. We confirmed that the converged curve is not significantly changed when smaller values of dt are used. This indicates that when s is less than 4, MSSG-Bin suffers from some spurious condensational growth, which artificially creates larger drops with larger fall velocities. TAU-Bin might suffer from some spurious growth as well. It is worth mentioning that TAU-Bin, which computes two moments of 34 bins, and MSSG-Bin(s2), which computes one moment of 66 bins, handle a similar amount of information and produce similar results for the duration of the buffer period at a similar computational cost, as shown in Table 1. The correspondence between these two models—developed by independent groups—gives extra confidence in their reliability.

Figure 4 shows vertical profiles of the rain mass mixing ratio Q_r at $t = 600$ s. Below 500 m, the 1-BULK models show significant values where the other models give little or no rain. This is again attributable to the overestimate of the autoconversion rate in the 1-BULK models. The three bin model results—TAU-Bin, MSSG-Bin(s1), and MSSG-Bin(s4)—are very small and barely visible in the figure. Figure 4c also includes the bin results at $t = 900$ s (dashed lines). The TAU-Bin and MSSG-Bin(s4) results at $t = 900$ s are similar to those of the two 2-BULK models [Thompson(2M) and WDM6] at $t = 600$ s. This indicates that the 2-BULK models successfully predict the rain profile but still overestimate the rain autoconversion rate. Some spurious growth makes the values in TAU-Bin and MSSG-Bin(s1) larger than those in MSSG-Bin(s4).

Figure 5 shows the surface rain rate for the KiD shallow convective cloud case. The numbers in brackets are the time durations T_{rain} for which the surface rain rate exceeds one-fifth of its maximum. The 1-BULK models fail to produce the onset time of surface rain, and produce shorter rain durations compared to the BIN models. The 2-BULK models produce better onset times, but with a somewhat shorter duration of rain than the 1-BULK models. This behavior is also seen in Shipway and Hill (2012), who adopted a different set of models, and can be attributed to the sedimentation calculations (Wacker and Seifert 2001; Stevens and Seifert 2008).

To confirm this behavior, a simple 1D sedimentation test was performed. Similar tests were conducted in Wacker and Seifert (2001) and Stevens and Seifert (2008), where a square pulse–like distribution of the initial rain mass was adopted. Here, on account of the smooth distribution shapes in Fig. 4, we adopted a smooth Gaussian distribution. The initial rain mass was distributed as

$$\rho_d Q_r(z, t = 0) = \begin{cases} Q_0 \exp\left[-\dfrac{(z - h_1)^2}{2\sigma_h^2}\right] & \text{for} \quad z \geq h_2 \\ 0 & \text{for} \quad z < h_2 \end{cases}, \tag{25}$$

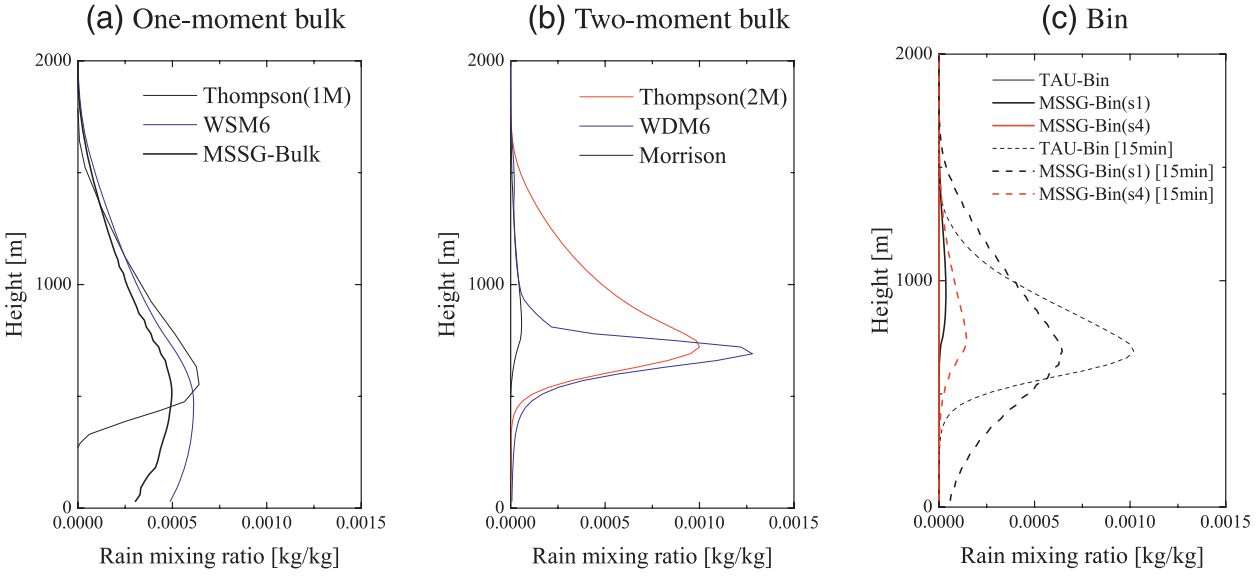

FIG. 4. (a),(b) Profiles of rain mixing ratio at $t = 600$ s for the KiD shallow convective cloud case. (c) As in (a),(b), but also with profiles at $t = 900$ s (dashed lines).

where ρ_d was fixed at 1 kg m^{-3}, $Q_0 = 10^{-5}$ kg kg^{-1}, $h_1 = 800$ m, $h_2 = 500$ m, and $\sigma_h = 50$ m. The sedimentation process was calculated using both one-moment and two-moment bulk methods, and by the bin method. For the two-moment bulk method the initial number concentration of rain N_r was set to $N_r(z,0) = [\rho_d Q_r(z,0) N_{0r}^3/(\pi\rho_w)]^{1/4}$, with N_{0r} initially set to 8×10^6 and then prognosed by the model. For the one-moment bulk method, N_{0r} was held at 8×10^6 throughout. For the bin method, the initial distribution was given the exponential form $dN_r = N_{0r} \exp(-\lambda_r D_r)$, with the slope parameter given by $\lambda_r = [\pi\rho_w N_{0r}/\rho_d Q_r(z,0)]^{1/4}$. These settings give the same initial number concentrations across all of the models. The precipitation component of MSSG-Bin was used, but with the sedimenting velocity assumed to take the power-law form $U_r(D_r) = a_r D_r^{b_r} (\rho_0/\rho_a)^{1/2}$ to match the bulk methods. Note that 132 bins were used ($s = 4$), and due to this high bin resolution conservation of the

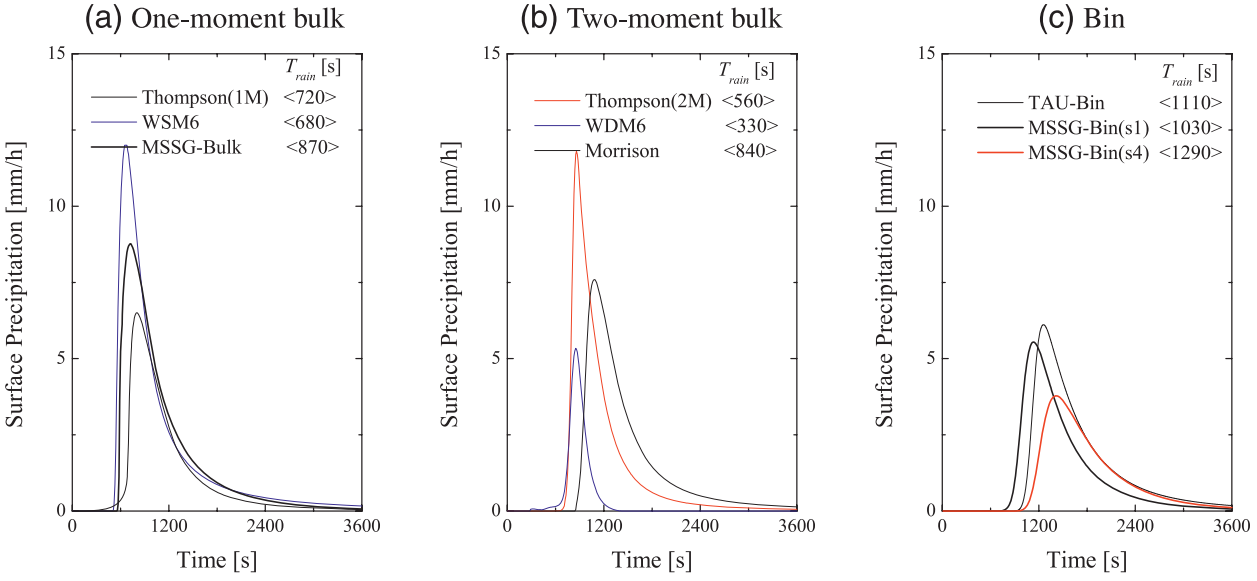

FIG. 5. Surface rain rate for the KiD shallow convective cloud case. The numbers in brackets are the time durations T_{rain} for which the surface rain rate exceeds one-fifth of its maximum.

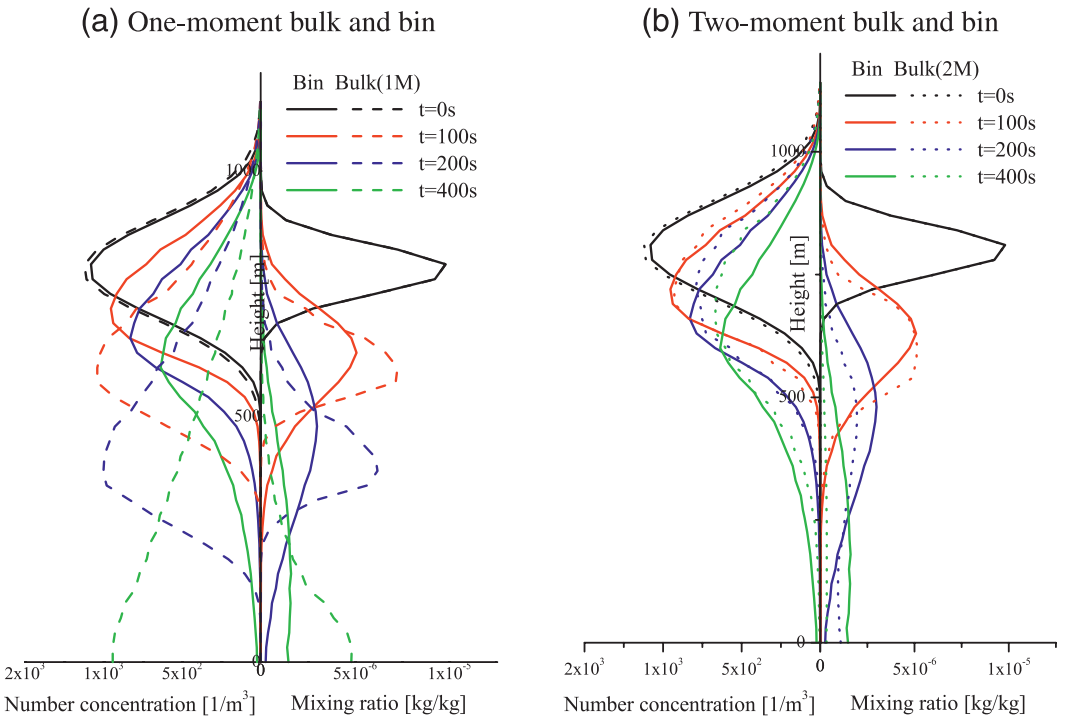

FIG. 6. Sedimenting number and mass concentrations for the simple precipitation test.

diagnosed number concentration was maintained to eight digits until the first rain drops reached the surface. The number concentration and mixing ratio from the bin method is therefore considered as a reference.

Figure 6 shows vertical profiles of sedimenting number concentration and liquid mixing ratio for the simple sedimentation test. (The number concentrations for the bin and one-moment bulk methods were diagnosed.) Figure 6a shows significant differences between the one-moment and bin results. In contrast, the two-moment and bin results are much closer (Fig. 6b). However, a close look at the profiles for t =400 s reveals significant differences. The number concentration for the two-moment method is much smaller than for the bin method near the surface, which leads to unreasonably large diagnosed rain drops.

Figure 7 shows the surface rain rate for the simple sedimentation test. As in Fig. 5, the numbers in brackets are the durations for which the surface rain rate exceeds one-fifth of its maximum. The one-moment bulk method cannot provide the correct onset of rainfall, but the two-moment method can. It should be noted, however, that the two-moment bulk method fails to predict the long duration of rainfall given by the bin method, giving a duration shorter even than the one-moment method. This test clearly shows a fundamental problem applying even to two-moment bulk schemes. This test adopted a simple two-moment bulk method with an exponential size distribution and is therefore not an exact representation of current two-moment methods. For example, a gamma size distribution of the form $dN_r = N_{0r} D_r^{\mu} \exp(-\lambda_r D_r)\, dD_r$ with a diagnostic shape parameter μ improves the simulation of sedimentation (Milbrandt and Yau 2005a; Stevens and Seifert 2008). However, the fact that a very similar tendency is still seen in Fig. 5 shows that current two-moment models still suffer from this fundamental problem. Another fundamental problem

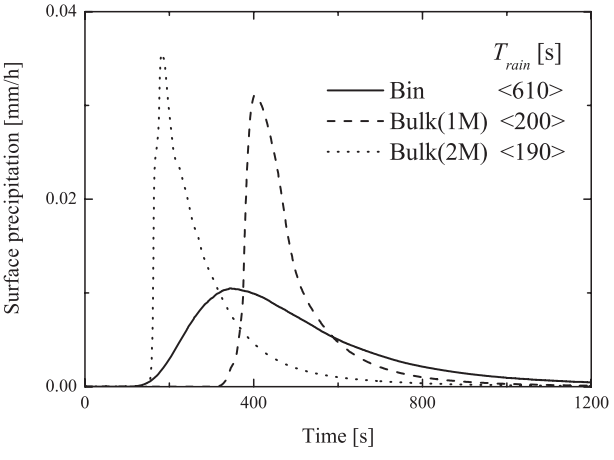

FIG. 7. Surface rain rate for the simple sedimentation test. The numbers in brackets are the time durations T_{rain} for which the surface rain rate exceeds one-fifth of its maximum.

of bulk models was reported in Li et al. (2009), which demonstrated unphysical enhanced rain evaporation in bulk models. The bin treatment has clear advantages for such issues.

c. Deep convection case

Case 10 in KiD has been developed as a steady-state test of deep convection. A constant-in-time height-dependent updraft is applied to the hydrometeors (not water vapor or temperature) and a constant-in-time height-dependent source term applied for water vapor, with magnitude chosen such that a steady rain rate of f_{q1} can be expected. The forms for the updraft and the vapor forcing are

$$w(z,t) = \begin{cases} w_1 \cos^4\left(\dfrac{\pi}{2}\dfrac{z - 5000}{5000}\right) & \text{for} \quad |z - 5000| < 5000 \\ 0.0 & \text{otherwise} \end{cases} \tag{26}$$

and

$$\left.\frac{dq}{dt}\right|_{\text{force}}(z,t) = \left.\frac{dq}{dt}\right|_{\text{force}}(z,0) = \begin{cases} A \cos^2\left(\dfrac{\pi}{2}\dfrac{z - 7000}{7000}\right) & \text{for} \quad |z - 7000| < 7000 \\ 0.0 & \text{otherwise} \end{cases}, \tag{27}$$

where A satisfies

$$\int_0^{z_1} \left.\frac{dq}{dt}\right|_{\text{force}}(z,0)\, dz = f_{q1}/3600. \tag{28}$$

The parameter settings are $z_1 = 15\,000$ m, $w_1 = 10$ m s^{-1}, and $f_{q1} = 5$ mm h^{-1}. The duration and depth of the simulations are 12 h and 15 000 m, respectively.

For this case, the temperature profile is dry adiabatic and the vapor mixing ratio profile is constant until the saturation level is reached. Above this level the temperature profile is pseudoadiabatic and the vapor saturated. At temperatures below 273.15 K, the vapor is saturated with respect to ice. At the surface, the temperature, pressure and water vapor mixing ratio are 300 K, 1000 hPa, and 18 g kg^{-1}, respectively. While the vapor field evolves via the source term and microphysical tendencies, it is not advected. The temperature field is held fixed for all time.

Table 2 shows the model descriptions and FPO ratios for the deep convection test case. TAU-Bin is not shown in this subsection because it does not provide a component for cold cloud. As in Table 1, the 2-BULK models require several tens of percent more FPOs than the 1-BULK models. MSSG-Bin(s1) with SDI—hereafter referred to as MSSG-Bin[SDI]—requires approximately 10 times more FPOs than the bulk models, with MSSG-Bin[SDI](s4) and MSSG-Bin[SII](s4) requiring a further factor of about 5. The huge computational costs incurred by the MSSG-Bin(s4) models are partly due to this being a 1D simulation, where all the grid boxes at cloudy altitudes have cloud condensates and therefore require cloud microphysical calculations. In 3D simulations, not all the grid boxes will have cloud condensates and consequently the computational load is somewhat smaller, as we will see in section 4.

Figure 8 shows the vertical profiles of hydrometeor mass mixing ratio for the deep convection case at 6 h. Because they use the same bulk model for ice-phase processes, MSSG-Bin[SDI] and MSSG-Bin[SDI](s4) differ significantly only for liquid water (i.e., cloud and rainwater). The rain mixing ratio is slightly larger in MSSG-Bin[SDI] than in MSSG-Bin[SDI](s4) because insufficient size resolution causes artificial numerical growth. The cloud mixing ratio in MSSG-Bin[SDI] is consequently smaller than in MSSG-Bin[SDI](s4). All of the hydrometeor profiles for the MSSG-Bin models are within the range spanned by the other models. In particular, it should be noted that the overlap of the liquid and solid water profiles at $6000 < z < 8000$ m is well represented in the MSSG-Bin models. This confirms the applicability of MSSG-Bin to deeply convective clouds.

Figure 9 shows the impact of the hybrid interface on the results. Three interfaces are tested. The first, referred to as SDI(40 μm), uses the SDI, with the cutoff radius (which divides cloud droplets and rain drops) set to 40 μm. The second, referred to as SII(40 μm), uses the SII with $r_{\text{cutoff}} = 40$ μm, and the third, referred to as SDI(100 μm), uses the SDI with $r_{\text{cutoff}} = 100$ μm. Figure 9a shows the vertical profiles of hydrometeor mass mixing ratio for the different interfaces. Differences are mainly seen at the altitudes where there is an overlap of liquid and solid water. The graupel mixing ratio is larger for the SDI experiments than for the SII experiment, while the cloud, rain, and snow mixing ratios are smaller. The processes P_{gacw} (graupel generation due to the collection of cloud water by graupel) and P_{gacr} (graupel generation due to the collection of rainwater by graupel) were significantly larger for the SDI experiments (not shown), which led to larger graupel mixing ratios and smaller cloud and rain mixing ratios. These smaller cloud mixing ratios led to smaller values of $P_{\text{s.sacw}}$ (snow generation due to the collection of cloud water by

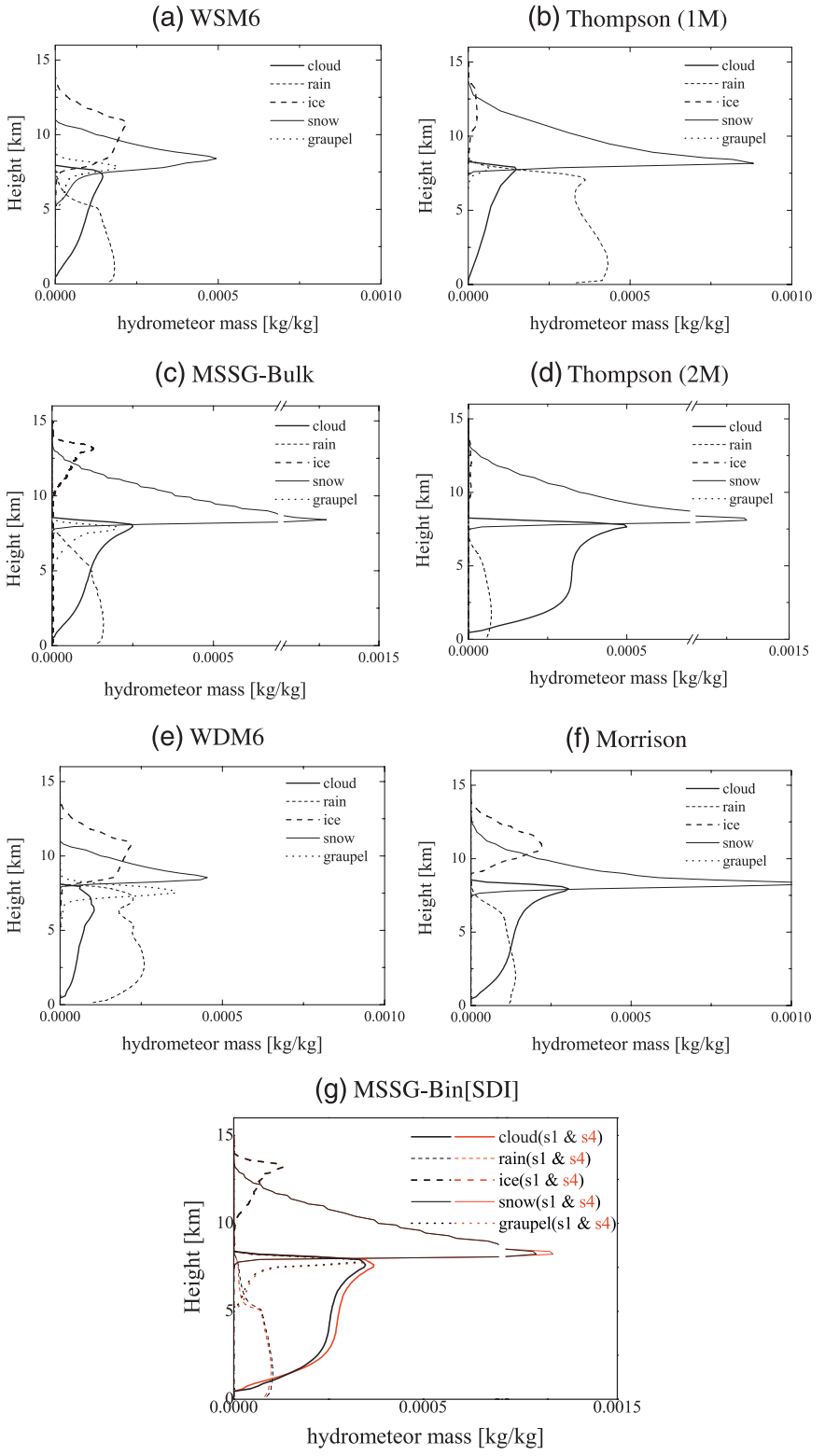

FIG. 8. Vertical profiles of hydrometer mass mixing ratio for the deep convection case at 6 h for (a) WSM6, (b) Thompson(1M), (c) MSSG-Bulk, (d) Thompson(2M), (e) WDM6, (f) Morrison, and (g) MSSG-Bin with the size-dependent interface (SDI).

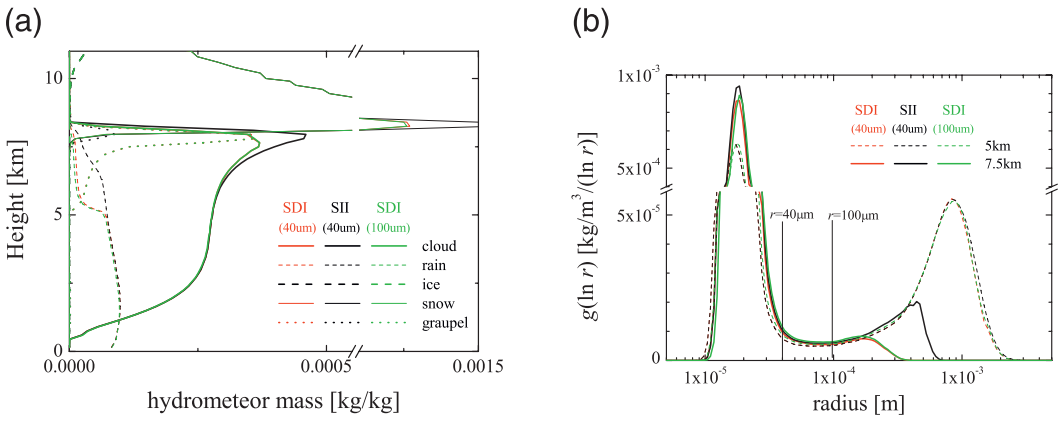

FIG. 9. Impact of the hybrid interface on (a) vertical profiles of hydrometer mass mixing ratios and (b) liquid droplet size distributions at 7.5- and 5-km altitude for the deep convection case at 6 h.

snow) resulting in smaller snow mixing ratios for the SDI experiments. There are only small differences between SDI(40 μm) and SDI(100 μm). This is well illustrated by the bimodal size distributions shown in Fig. 9b, which show the liquid droplet size distribution at 7.5 and 5 km. There is little mass in the range $40 < r < 100$ μm, resulting in a small influence of the variance of r_{cutoff} in this range. In Fig. 9a, we see a large difference in mixing ratios between the SDI and SII experiments at 7.5 km, but little difference at 5 km. The same pattern is seen in the size distributions. The large difference in the size distribution at 7.5 km is in the large-drop regime $r >$ 100 μm. Large drops over 300 μm are selectively depleted by graupel in the SDI. The diagnosed mean radius of rain in the bulk treatment using the SII was smaller than the actual mean, which led to less efficient depletion of rain by graupel. Interestingly, this large difference at 7.5 km disappears at 5 km. It should be noted, however, that this is largely due to the kinematic framework, which shuts off the feedbacks between cloud microphysics and dynamics. With the feedbacks included, the differences in latent heat release due to the different ratios of solid and liquid water would make a difference to the dynamics, which would consequently affect the hydrometeor masses.

4. 3D intercomparison experiments

a. RICO model intercomparison

The RICO precipitating shallow cumulus case is based on data obtained during the successful Rain in Cumulus over the Ocean measurement campaign, which took place in the vicinity of the Caribbean islands Antigua and Barbuda during December 2004–January 2005. For this study, we ran shallow cumulus simulations following the protocol of the RICO model intercomparison project (http://www.knmi.nl/samenw/rico/). As shown in Fig. 10, the domain size is $12.8 \times 12.8 \times 4.0$ km^3 with $128 \times 128 \times 100$ grid boxes, implying $dx = dy = 100$ m and $dz = 40$ m. Periodic conditions are imposed on the lateral boundaries. To minimize spurious reflection of upward-propagating gravity waves, we followed the recommendation to incorporate a sponge layer near the top boundary in order to damp the perturbations. Momentum and sensible and latent heat fluxes are parameterized using typical maritime values of the surface roughness. The simulation duration was 24 h, with analysis confined to the last 4 h. Large-scale forcings were applied to the moisture, heat, and velocity fields in order to achieve a quasi-steady state during the analysis period.

Table 3 shows the list of models, details of which can be found in appendix B of Ackerman et al. (2009) and in section 2.3 of van Zanten et al. (2011).

b. Model intercomparison results

Figure 11 shows time series of LWP and RWP for the various models. Judging from the intermodel averages denoted by the thick dotted lines, the RICO models

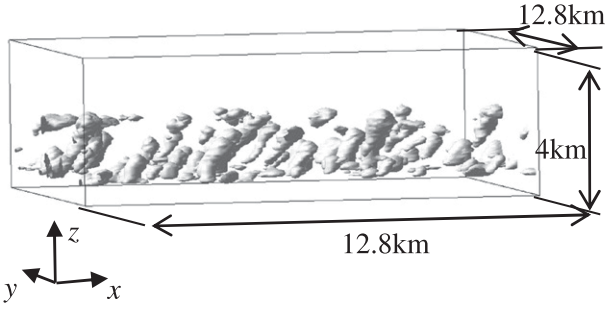

FIG. 10. Computational domain for the RICO model intercomparison. A cloud mixing ratio simulation from MSSG-Bulk is shown as an example.

TABLE 3. RICO model references.

	Model name	Authors
One-moment	Regional Atmospheric Modeling System at Colorado State University (RAMS-CSU)	W. Cheng
	Nonhydrostatic Mesoscale atmospheric model (MESO-NH)	F. Couvreux
	Utah model (Utah)	P. A. Bogenschuts and S. Krueger
	Japan Agency for Marine–Earth Science of Technology (JAMSTEC)	A. Noda and K. Nakamura
	System for Atmospheric Modeling (SAM)	M. Khairoutdinov
	Eulerian/Lagrangian cloud model (EULAG)	J. Slawinska, A. Wyszogrodzki, and W. W. Grabowski
	Bulk component of the Multi-Scale Simulator for the Geoenvironment (MSSG-Bulk)	See appendixes A and B
Two-moment	West Virginia University model (WVU)	D. C. Lewellen
	U of California, Los Angeles model (UCLA)	B. Stevens
	Coupled Ocean–Atmosphere Mesoscale Prediction System (COAMPS)	S. Wang
	United Kingdom Meteorological Office (UKMO)	B. Shipway
	Dutch Atmospheric Large-Eddy Simulation model (DALES)	M. C. van Zanten
Bin	Distributed Hydrodynamic Aerosol and Radiative Modeling Application (DHARMA)	A. Ackerman
	NOAA Regional Atmospheric Modeling System (RAMS-NOAA)	H. Jiang
	System for Atmospheric Modeling with Explicit Microphysics (SAMEX)	D. Mechem and Y. Kogan
	Bin component of the Multi-Scale Simulator for the Geoenvironment with $s = 1$ [MSSG-Bin(s1)]	Present model, 33 bins
	Bin component of the Multi-Scale Simulator for the Geoenvironment with $s = 4$ [MSSG-Bin(s4)]	Present model, 132 bins

successfully achieve a quasi-steady state for the last 4 h of the 24-h simulations, as designed. Although the MSSG models tend to produce less liquid water than the intermodel average, irrespective of microphysical scheme, they are still within the range spanned by the other models. The RWP of MSSG-Bin(s4) shows the lowest value among the BIN models. However, it is comparable to the RWP of the National Oceanic and Atmospheric Administration's (NOAA's) Regional Atmospheric Modeling System (RAMS).

Figure 12 shows vertical profiles of rain Q_r for the various models. The altitudes of maximum Q_r vary from 700 to 2000 m in the 1-BULK models but are concentrated around 2000 m in the 2-BULK and BIN models. The lower altitudes of maximum Q_r in the 1-BULK models can be attributed again to the overestimate of

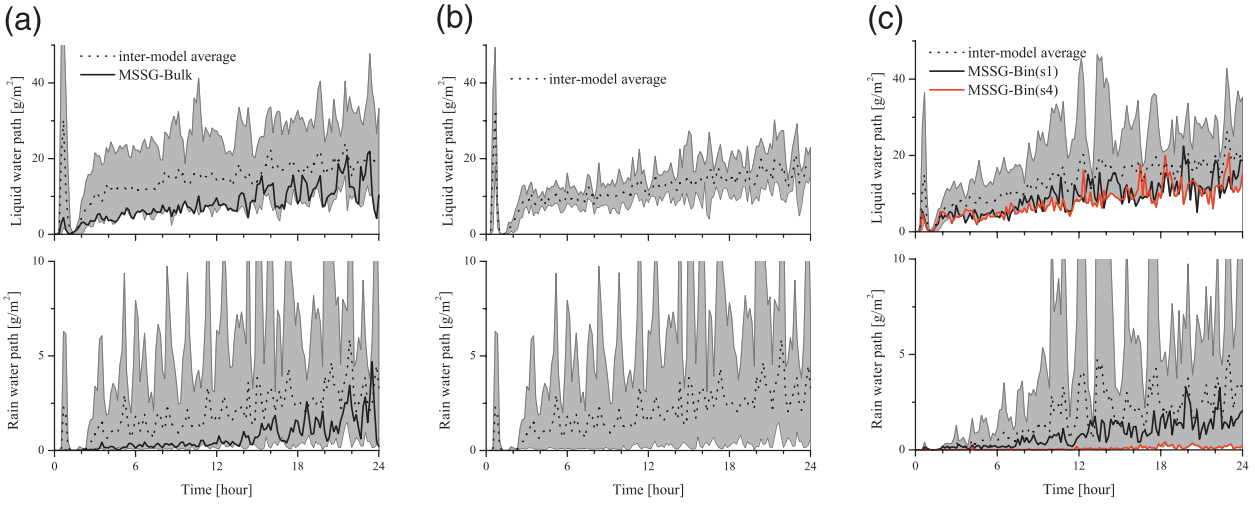

FIG. 11. Liquid water path and rainwater path for (a) one-moment bulk models, (b) two-moment bulk models, and (c) bin models. The intermodel spread is given by the shading.

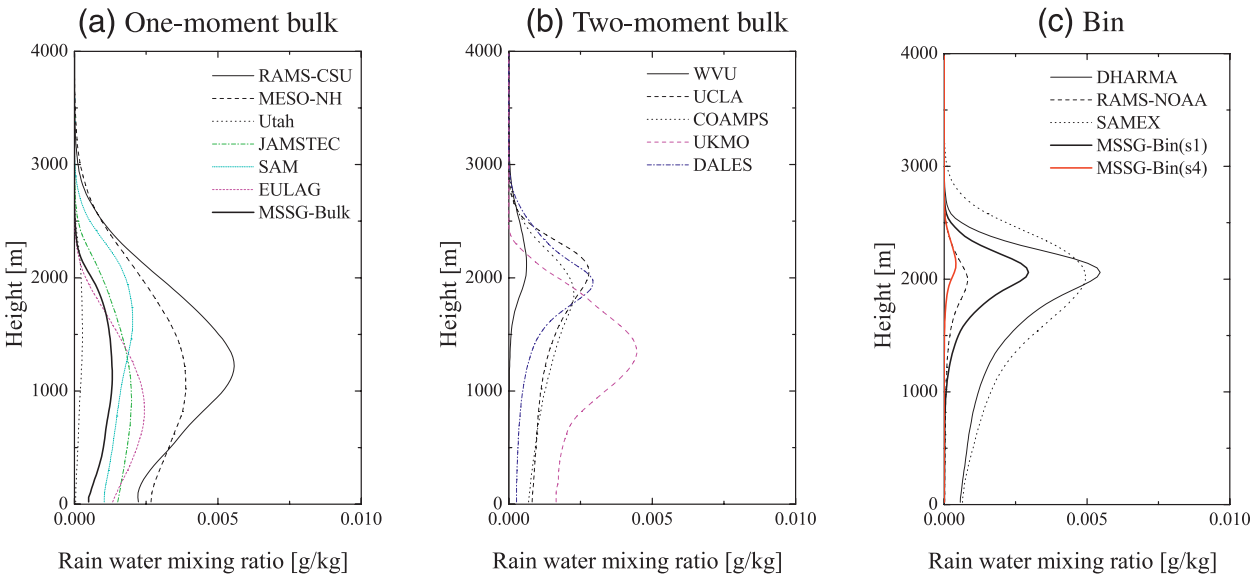

FIG. 12. Vertical profiles of rain mixing ratio for (a) one-moment bulk models, (b) two-moment bulk models, and (c) bin models.

the autoconversion rate, as discussed in section 3b. Although the BIN models show a consistent altitude of maximum Q_r, the values at the maximum vary widely. One possible reason for these differences is artificial numerical growth at low bin resolutions. We suspect this is the reason for the difference between MSSG-Bin(s1) and MSSG-Bin(s4).

Figure 13 shows vertical profiles of total liquid mixing ratio Q_l (i.e., cloud plus rain). For four of the 1-BULK models, the altitude of maximum Q_l is located at the cloud base ($z \sim 700$ m), while for all but the Met Office (UKMO) model, the 2-BULK and BIN models give maxima at the cloud top ($z \sim 2000$ m). Interestingly, excepting the UKMO model, the variability between models is smallest among the 2-BULK models (smaller than for the BIN models). This does not mean, however, that the 2-BULK models are more reliable. Currently BIN models have many options for, for example,

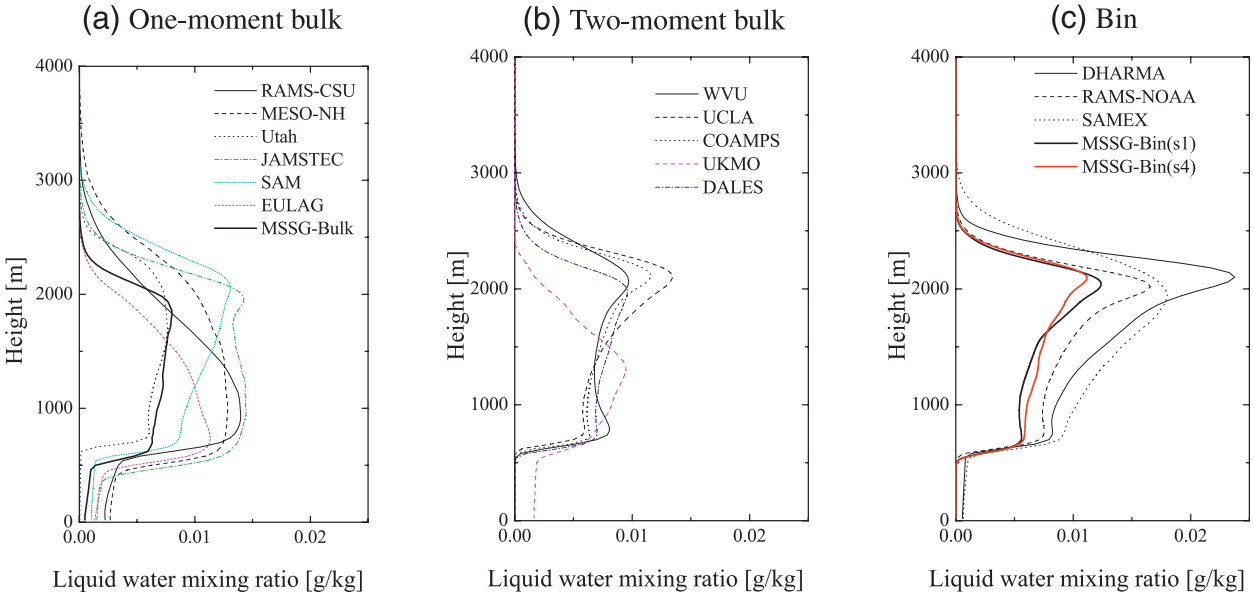

FIG. 13. As in Fig. 12, but for liquid water mixing ratio.

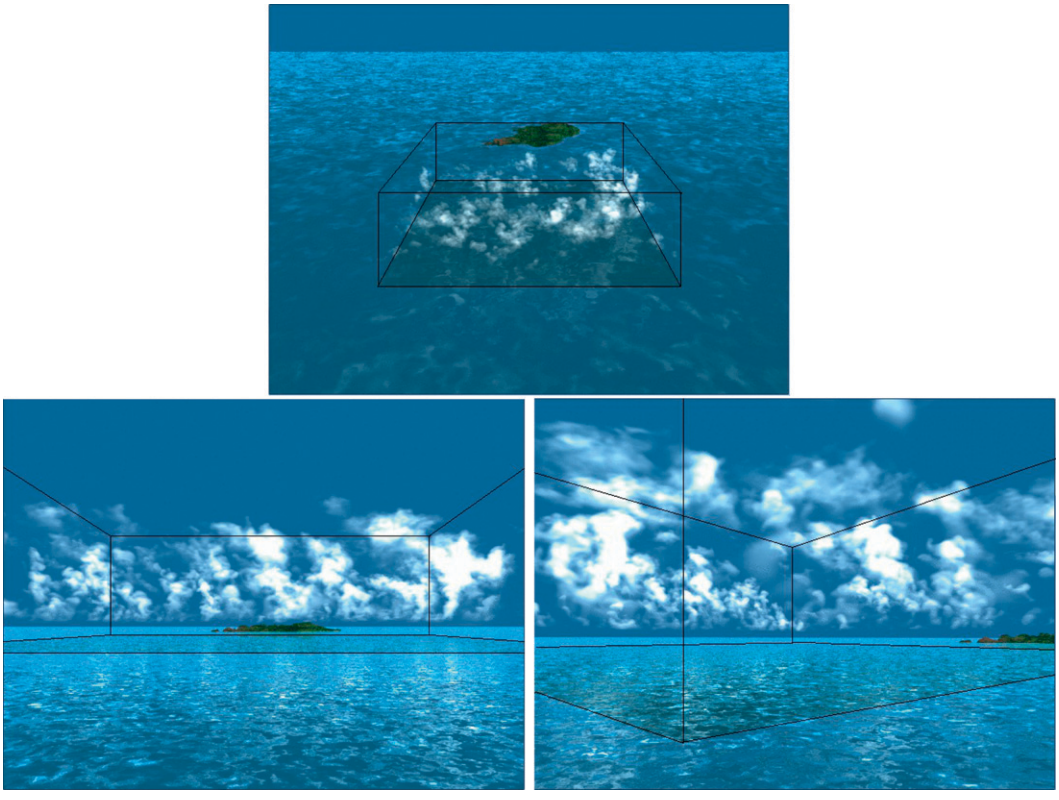

FIG. 14. 25-m-resolution simulation using the RICO model intercomparison protocol. A ray-tracing technique is employed to calculate the Mie scattering, depending on droplet size. The superimposed solid lines indicate the domain boundaries, and an artificial island, with length 8 km, width 5 km, and height 0.5 km, is shown to provide a size reference. The movie is available online.

aerosol type, collision, and breakup kernel type. The choices for these options cause more quantitative differences between the BIN models than between the 2-BULK models.

c. 25-m-resolution simulation

The RICO simulation protocol suggests resolutions of $dx = dy = 100$ m and $dz = 40$ m. However, the 100-m horizontal resolution is not sufficient to resolve turbulent entrainment at the cloud edge. Turbulent entrainment is one of the mechanisms able to induce a quick rain initiation (Krueger et al. 1997) and is a longstanding issue in studies of cloud microphysics. Here, we describe a very high-resolution simulation using the MSSG-Bin model. The domain size was kept the same as that specified by the RICO protocol (i.e., $12.8 \times 12.8 \times 4.0$ km^3) but the number of grid boxes was increased to $512 \times 512 \times 200$, yielding $dx = dy = 25$ m and $dz = 20$ m. The initial data were created by linearly interpolating the data from the 100-m-horizontal-resolution simulation at 24 h. A 1-h simulation was then performed on the very high-resolution grid, with the first half-hour discarded and the last half-hour used to create visualizations. A movie visualization for this period is available online, and three frames are shown in Fig. 14. Small-scale structures due to turbulent entrainment—absent from the 100-m-resolution simulation shown in Fig. 10—are clearly captured. This confirms the feasibility of MSSG-Bin for high-resolution simulations, but we will postpone detailed discussion to future studies.

d. Computational cost

The RICO simulations with MSSG-Bulk and MSSG-Bin were performed on the Earth Simulator 2 (ES2), which is a vector-type supercomputer at JAMSTEC consisting of 160 nodes (NEC-SX-9/E with eight CPUs in each node) with a peak performance of 131 TFLOPS.

The MSSG-Bulk simulation was performed on four nodes of ES2, and took 2.7 h and 1.9 PFLO (peta floating-point operations) to complete the 40 200 time steps required for the 24-h RICO simulation. The MSSG-Bin(s1) and (s4) simulations were run on eight nodes and took 5.7 h (9.4 PFLO) and 21.1 h (36.7 PFLO) to complete 38 500 and 39 200 time steps, respectively. The ratio

of the required number of FPOs between MSSG-Bin(s1) and MSSG-Bulk is 4.9, which is smaller than the ratio of 8.3 shown in Table 1. Similarly, the ratio of MSSG-Bin(s4) to MSSG-Bulk is 32.4, compared to 50.7 in the table. These reductions are attributable to two differences between the three-dimensional RICO and one-dimensional kinetic simulations. One is that the RICO simulations include model dynamics calculations, which are not required in the kinetic simulations. The cost of the dynamics calculations is similar in the MSSG-Bin and MSSG-Bulk simulations and as a consequence dilutes the cost for the bin microphysical calculations. The other is that the ratio of cloudy to noncloudy grid boxes is smaller in the 3D simulations compared to the 1D simulations.

The very-high-resolution case with MSSG-Bin(s1) in the previous subsection was performed on 32 nodes, taking 1.8 h for the 1-h simulation. The MSSG model scales well on the Earth Simulator system (Takahashi et al. 2005). If we use all of the system (i.e., 160 nodes) the elapsed time reduces by a factor of 5. Thus, even at these very high resolutions it is quite feasible to perform multiple simulations with MSSG-Bin.

5. Conclusions

This study describes a bin–bulk hybrid cloud microphysical model named MSSG-Bin, in which warm-rain processes are calculated using a spectral bin formulation and cold-rain processes using a bulk formulation. The hybrid system provides accurate simulations of liquid droplet growth, free from the approximations made in bulk parameterizations. The bulk formulation for cold-rain processes avoids the uncertainties in the governing equations for complex-shaped ice particles. The authors believe that this kind of hybrid approach provides an attractive alternative to the so-called full spectral bin models, which consume greater computational resources but still require tuning parameters for cold-rain processes.

Two types of interface between the bin and bulk components have been proposed and implemented within the model. One sums up the mass within the bins to provide cloud water and rainwater mixing ratios for interaction with the ice categories. After the ice-phase processes have been computed, the changes due to the warm–cold interactions are remapped to the bins in proportion to the original mass within them. Since the size distribution across the bins is discarded, we call this the size-independent interface (SII). The other interface keeps the size information and computes the interaction between each bin and the ice categories separately. We call this the size-dependent interface (SDI). Since the computational costs are almost the same, there is no reason to use the SII in preference to the SDI. However, the comparison between the SII and SDI provides insight into the sensitivity to the hybrid interface.

MSSG-Bin has been compared with other models using standard 1D and 3D model intercomparison frameworks for shallow and deep convective clouds. The kinematic framework named KiD was used for the 1D intercomparisons and the Rain In Cumulus over the Ocean (RICO) model intercomparison framework for the 3D simulations. These intercomparisons confirm the reliability of MSSG-Bin for shallow clouds and its applicability to deeply convective clouds. A supplementary test for simple sedimenting hydrometeors confirms the advantage of the bin treatment compared to both one- and two-moment bulk models.

Compared with MSSG-Bulk, MSSG-Bin with $s = 1$ (i.e., 33 bins) requires 8.3 times more floating-point operations (FPOs) for the one-dimensional shallow convection case but only 4.9 times more for the RICO case, and we have demonstrated the feasibility of using the model for a 25-m-resolution simulation of shallow cumulus on a $512 \times 512 \times 200$ grid. It has been confirmed that the MSSG-Bin simulations converge for $s \geq 4$. The required number of FPOs for MSSG-Bin with $s = 4$ is about 50 times larger than for the bulk models for the 1D warm-rain simulations, but only 32 times larger for the 3D simulations. It is therefore feasible to run MSSG-Bin with $s = 4$ for simulations of 3D mesoscale clouds and thus obtain reliable reference results.

Acknowledgments. The 3D simulations were performed on the Earth Simulator 2 at the Japan Agency for Marine-Earth Science and Technology. The research was partly supported by the Science and Technology Research Partnership for Sustainable Development (SATREPS) project of the Japan Science and Technology Agency (JST). We thank all those who participated in KiD and RICO and provided the data and source code that made this study possible. We would also like to sincerely thank Mr. Adam Clayton and Dr. Ben Shipway for their helpful comments on the manuscript.

APPENDIX A

Bulk Parameterizations for Ice-Phase Processes in the MSSG-Bin Model

The terms for cloud ice, snow, and graupel are described in Tables A1, A2, and A3, respectively. MSSG-Bin uses the same equations for solid water as the MSSG-Bulk model.

TABLE A1. Production terms for cloud ice.

Notation	Description	Reference
P_{idsn}	Generation rate of ice by nucleation of ice (s^{-1})	Eq. (A.21) in Reisner et al. (1998)
P_{ifzc}	Generation rate of ice by homogeneous and heterogeneous freezing of cloud water (s^{-1})	Eqs. (A.22) and (A.23) in Reisner et al. (1998)
P_{ispl}	Generation rate of ice by the ice splinter multiplication process (s^{-1})	Eq. (A.25) in Reisner et al. (1998) with modification by Thompson et al. (2004)
P_{idep}	Generation rate of ice by depositional growth of ice (s^{-1})	Eq. (A.26) in Reisner et al. (1998)
P_{iacw}	Collection rate of cloud water by ice (s^{-1}). Used for $P_{i.iacw}$ and $P_{g.iacw}$ calculations.	Eq. (A.27) in Reisner et al. (1998)
$P_{i.iacw}$	Generation rate of ice by only a portion of cloud water which is collected by ice (s^{-1})	Eq. (A.28) in Reisner et al. (1998)
N_{iag}	Reduction rate of N_i by aggregation of cloud ice (m^{-3} s^{-1})	Eq. (A.31) in Reisner et al. (1998)

TABLE A2. Production terms for snow.

Notation	Description	Reference
P_{icns}	Generation rate of snow by conversion of ice into snow (s^{-1})	Eq. (A.34) in Reisner et al. (1998)
P_{sdep}	Generation rate of snow by depositional growth of snow (s^{-1})	Eq. (A.36) in Reisner et al. (1998) with modification by Thompson et al. (2004)
P_{smlt}	Generation rate of rain by the melting of snow (s^{-1})	Eq. (A.37) in Reisner et al. (1998)
P_{saci}	Generation rate of snow due to the collection of ice by snow (s^{-1})	Eq. (A.38) in Reisner et al. (1998)
P_{sacw}	Collection rate of cloud water by snow (s^{-1}). Used for $P_{s.sacw}$ and $P_{g.sacw}$ calculations.	Eq. (A.46) in Reisner et al. (1998)
P_{sacr}	Collection rate of rain by snow (s^{-1}). Used for $P_{s.sacr}$ and $P_{s.sacr}$ calculations.	Eq. (A.47) in Reisner et al. (1998)
$P_{s.sacw}$	Generation rate of snow by that portion of the collected cloud water by snow which is converted into snow (s^{-1})	Eq. (A.45) in Reisner et al. (1998)
$P_{s.sacr}$	Generation rate of snow by that portion of the collected rain by snow which is converted into snow (s^{-1})	Eq. (A.53) in Reisner et al. (1998)

TABLE A3. Production terms for graupel.

Notation	Description	Reference
P_{icng}	Generation rate of graupel due to the collection of cloud water by ice (s^{-1})	Eq. (A.39) in Reisner et al. (1998)
N_{icng}	Reduction rate of N_g due to collection of cloud water by cloud ice (m^{-3} s^{-1})	Eq. (A.40) in Reisner et al. (1998)
P_{raci}	Generation rate of graupel due to the collection of ice by rainwater (s^{-1})	Eq. (A.41) in Reisner et al. (1998)
P_{iacr}	Generation rate of graupel due to the collection of rainwater by ice (s^{-1})	Eq. (A.42) in Reisner et al. (1998)
$P_{g.sacw}$	Generation rate of graupel by that portion of collected rain by snow which is converted into graupel (s^{-1})	Eq. (A.43) in Reisner et al. (1998) with modification by Thompson et al. (2004)
P_{scng}	Generation rate of snow by accretion of cloud water (s^{-1})	Eq. (A.44) in Reisner et al. (1998)
P_{racs}	Collection rate of snow by rain (s^{-1}). Used for $P_{g.racs}$ calculation.	Eq. (A.48) in Reisner et al. (1998) with modification by Thompson et al. (2004)
$P_{g.racs}$	Generation rate of graupel by that portion of collected cloud snow by rain which is converted into graupel (s^{-1})	Eq. (A.50) in Reisner et al. (1998)
$P_{g.scar}$	Generation rate of graupel by that portion of collected snow by rain which is converted into graupel (s^{-1})	Eq. (A.52) in Reisner et al. (1998) with modification by Thompson et al. (2004)
P_{gacr}	Generation rate of graupel due to the collection of rain by graupel (s^{-1})	Eq. (A.13) in Rutledge and Hobbs (1984)
P_{gfzr}	Generation rate of graupel by freezing of rain to form graupel (s^{-1})	Eq. (A.56) in Reisner et al. (1998)
P_{gdep}	Generation rate of graupel by deposition growth of graupel (s^{-1})	Eq. (A.57) in Reisner et al. (1998)
P_{gacw}	Generation rate of graupel by accretion of cloud water (s^{-1})	Eq. (A.59) in Reisner et al. (1998) with modification by Thompson et al. (2004)
$P_{g.iacw}$	Generation rate of graupel by that portion of collected cloud water by ice which is converted into graupel (s^{-1})	Eq. (A.28) in Reisner et al. (1998)

TABLE B1. Production terms for cloud water.

Notation	Description	Reference
P_{ccnd}	Generation rate of cloud water by condensation (s^{-1})	Eqs. (A.63)–(A.65) in Reisner et al. (1998)
P_{imlt}	Generation rate of cloud water by melting of ice (s^{-1})	Eq. (A.66) in Reisner et al. (1998)

TABLE B2. Production terms for rain.

Notation	Description	Reference
P_{racw}	Generation rate of rain due to the collection of cloud water by rain (s^{-1})	Eq. (A.61) in Reisner et al. (1998) with modification by Thompson et al. (2004)
P_{ccnr}	Generation rate of rain by conversion of cloud water into rain (s^{-1})	Eq. (A.60) in Reisner et al. (1998)
P_{smlt}	Generation rate of rain by the melting of snow (s^{-1})	Eq. (A.37) in Reisner et al. (1998)
P_{gmlt}	Generation rate of rain by melting of graupel and enhanced melting of graupel due to the collection of cloud water and rain (s^{-1})	Eq. (A.58) in Reisner et al. (1998) with modification by Thompson et al. (2004)

APPENDIX B

Warm-Rain Component of the MSSG-Bulk Model

The MSSG-Bulk model prognoses mixing ratios of cloud water, rain, cloud ice, snow, and graupel, and in addition the number density of cloud ice particles. Thus, MSSG-Bulk is a one-moment model for warm rain and a partial two-moment model for cold rain. The cold rain processes are described in Eqs. (10)–(13) and appendix A. The governing equations for cloud water and rain are written as

$$\frac{\partial \rho_d Q_c}{\partial t} = -\text{ADV}(\rho_d Q_c) + \text{DIV}(\rho_d Q_c) + \text{DIFF}(\rho_d Q_c) + \rho_d(-P_{\text{ccnr}} - P_{\text{racw}} + P_{\text{ccnd}} - P_{\text{ifzc}} - P_{\text{ispl}} - P_{\text{s,sacw}} - P_{\text{g.sacw}} - P_{\text{gacw}} - P_{\text{i.iacw}} - P_{\text{g.iacw}} + P_{\text{imlt}}), \tag{B1}$$

$$\frac{\partial \rho_d Q_r}{\partial t} = -\text{ADV}(\rho_d Q_r) + \text{DIV}(\rho_d Q_r) + \text{DIFF}(\rho_d Q_r) + \rho_d(P_{\text{racw}} + P_{\text{ccnr}} - P_{\text{revp}} - P_{\text{gfzr}} - P_{\text{iacr}} - P_{\text{s,sacr}} - P_{\text{g.sacr}} - P_{\text{gacr}} + P_{\text{smlt}} + P_{\text{gmlt}}) - U_r \frac{\partial \rho_d Q_r}{\partial x_3}, \tag{B2}$$

where the production terms are as described in Tables B1 and B2.

APPENDIX C

Size-Dependent Interface for Hybrid Processes

a. Freezing of water

According to Bigg (1953),

$$\left(\frac{dN_k}{dt}\right)_{\text{frz}} = N_k \frac{\overline{m_k}}{\rho_w} B' \exp[A'(T_0 - T) - 1], \tag{C1}$$

where $\overline{m_k} = M_k/N_k$, $B' = 100\ \text{m}^{-3}\ \text{s}^{-1}$ and $A' = 0.66\ \text{K}^{-1}$. We then have

$$\left(\frac{dM_k}{dt}\right)_{\text{frz}} = \overline{m_k}\left(\frac{dN_k}{dt}\right)_{\text{frz}}. \tag{C2}$$

Frozen small droplets become cloud ice, and frozen large drops become graupel:

$$\rho_d P_{\text{ifzc}} = \sum_{k=1}^{n_{\text{cloud}}} \left(\frac{dM_k}{dt}\right)_{\text{frz}}, \tag{C3}$$

$$\rho_d P_{\text{gfzr}} = \sum_{k=n_{\text{cloud}}+1}^{n_{\text{bin}}} \left(\frac{dM_k}{dt}\right)_{\text{frz}}. \tag{C4}$$

When $T < 233.15$ K, any cloud water is homogeneously and instantly frozen to form cloud ice:

$$\left(\frac{dM_k}{dt}\right)_{\text{frz}} = \frac{M_k}{\Delta t} \quad \text{for} \quad k \le n_{\text{cloud}}, \tag{C5}$$

$$\rho_d P_{\text{ifzc}} = \frac{1}{\Delta t} \sum_{k=1}^{n_{\text{cloud}}} M_k = \rho_d Q_c / \Delta t. \tag{C6}$$

b. Melting of ice particles

If cloud ice is present at $T > T_{\mathrm{frz}}$, it is melted instantly (i.e., $P_{\mathrm{imlt}} = q_i/\Delta t$). The melted mass is received by the corresponding class, with mean cloud ice mass $\overline{m_i} = \rho_d Q_i/N_i$:

$$\left(\frac{\partial M_{\mathrm{k.imlt}}}{\partial t}\right)_{\mathrm{imlt}} = \rho_d P_{\mathrm{imlt}} \quad \text{for} \quad m_{\mathrm{k.imlt}-1/2} < \overline{m_i} \le m_{\mathrm{k.imlt}+1/2}. \tag{C7}$$

Since melted cloud ice is moved to the cloud water category in the bulk scheme, class k.imlt is restricted such that $1 \le \mathrm{k.imlt} \le n_{\mathrm{cloud}}$.

The snowmelt per unit time P_{smlt} is calculated assuming an exponential distribution of snow particle sizes (Rutledge and Hobbs 1983; Reisner et al. 1998). This term, however, does not specify how many liquid droplets form from the melting snow. This study assumes that all melting snow is converted to liquid drops of mass $\overline{m_s}(=\rho_d Q_s/N_s)$,which is the mean mass of snow. As in the treatment of melting cloud ice, the melted mass is received by the corresponding class of liquid water:

$$\left(\frac{\partial M_{\mathrm{k.smlt}}}{\partial t}\right)_{\mathrm{smlt}} = \rho_d P_{\mathrm{smlt}} \quad \text{for} \quad m_{\mathrm{k.smlt}-1/2} < \overline{m_s} \le m_{\mathrm{k.smlt}+1/2}. \tag{C8}$$

The melting of graupel is treated in the same manner; that is,

$$\left(\frac{\partial M_{\mathrm{k.gmlt}}}{\partial t}\right)_{\mathrm{gmlt}} = \rho_d P_{\mathrm{gmlt}} \quad \text{for} \quad m_{\mathrm{k.gmlt}-1/2}\overline{m_g} \le m_{\mathrm{k.gmlt}+1/2}, \tag{C9}$$

where $\overline{m_g}(=\rho_d Q_g/N_g)$ is the mean mass of graupel. Since melted snow and graupel are moved to the rain category in the bulk scheme, classes k.smlt and k.gmlt are restricted such that $n_{\mathrm{cloud}} < \mathrm{k.smlt} \le n_{\mathrm{bin}}$ and $n_{\mathrm{cloud}} < \mathrm{k.gmlt} \le n_{\mathrm{bin}}$.

c. Collisions between water droplets/drops and ice particles

1) COLLISIONS BETWEEN LIQUID WATER AND CLOUD ICE

The collection of cloud ice by liquid water ice is given by

$$\left(\frac{dM_k}{dt}\right)_{\underline{\mathrm{k}}\mathrm{aci}} = \frac{\pi}{4}(\overline{D_i} + \overline{D_k})^2 E_{ik}|U_{di} - U_k|N_k\rho_d Q_i, \tag{C10}$$

where $U_{di} = 7 \times 10^2 \overline{D_i}$, $\overline{D_k} = (6\overline{m_k}/\pi\rho_w)^{1/3}$, and E_{ik} is the collection efficiency of cloud ice for liquid water, given by

$$E_{ik} = \begin{cases} 0.572 \times \log_{10}(\psi_k - 0.25) + 0.967 & (k \le n_{\mathrm{cloud}}) \\ 1 & (k > n_{\mathrm{cloud}}) \end{cases}, \tag{C11}$$

where $\psi_k = \overline{D_k}(\rho_w U_{di}/\phi\overline{D_i})^{1/2}$, with $\phi = 3.24 \times 10^{-4}$. Note that if $\psi_k < 0.25$, then $E_{ik} = 0$.

The collection of liquid water by cloud ice is similarly calculated as

$$\left(\frac{dM_k}{dt}\right)_{\mathrm{ac}\underline{\mathrm{k}}} = \frac{\pi}{4}(\overline{D_i} + \overline{D_k})^2 E_{ik}|U_{di} - U_k|N_i M_k. \tag{C12}$$

The corresponding bulk quantities are given by

$$\rho_d P_{\mathrm{iacw}} = \sum_{k=1}^{n_{\mathrm{cloud}}} \left(\frac{dM_k}{dt}\right)_{\mathrm{ac}\underline{\mathrm{k}}}, \tag{C13}$$

$$\rho_d P_{\mathrm{iacr}} = \sum_{k=n_{\mathrm{cloud}}+1}^{n_{\mathrm{bin}}} \left(\frac{dM_k}{dt}\right)_{\mathrm{ac}\underline{\mathrm{k}}}, \tag{C14}$$

$$\rho_d P_{\mathrm{raci}} = \sum_{k=n_{\mathrm{cloud}}+1}^{n_{\mathrm{bin}}} \left(\frac{dM_k}{dt}\right)_{\underline{\mathrm{k}}\mathrm{aci}}. \tag{C15}$$

For consistency with the bulk scheme, wherever collection of cloud ice by cloud water (P_{waci}) is ignored, $(dM_k/dt)_{\underline{\mathrm{k}}\mathrm{aci}}$ is not calculated for $k \le n_{\mathrm{cloud}}$.

2) COLLISIONS BETWEEN LIQUID WATER AND SNOW

Cloud droplets are assumed to be much smaller than snow particles. Thus, for $k \le n_{\mathrm{cloud}}$,

$$\begin{aligned}\left(\frac{dM_k}{dt}\right)_{\mathrm{sac}\underline{\mathrm{k}}} &= \overline{m_k}\int_0^\infty \frac{\pi}{4}\overline{D_s}^2 E_{sk} U_s(D_s) N_k N_{0s} \exp(-\lambda_s D_s)\, dD_s \\ &= \frac{\pi}{4} N_{0s} M_k E_{sk} \times a_s \frac{\Gamma(b_s + 3)}{\lambda_s^{b_s+3}}.\end{aligned} \tag{C16}$$

For $k > n_{\mathrm{cloud}}$, the size of rain drops is considered:

$$\left(\frac{dM_k}{dt}\right)_{\text{sac}\underline{\text{k}}} = \overline{m_k}\int_0^\infty \frac{\pi}{4}(\overline{D_s} + \overline{D_k})^2 E_{sk}|U_s(D_s) - U_k|N_k N_{0s}\exp(-\lambda_s D_s)\,dD_s$$
$$= \frac{\pi}{4}N_{0s}M_k E_{sk} \times \left| a_s\left[\frac{\Gamma(b_s+3)}{\lambda_s^{b_s+3}} + 2\overline{D_k}\frac{\Gamma(b_s+2)}{\lambda_s^{b_s+2}} + \overline{D_k}^2\frac{\Gamma(b_s+1)}{\lambda_s^{b_s+1}}\right] - V_k\left(\frac{2}{\lambda_s^3} + \frac{2\overline{D_k}}{\lambda_s^2} + \frac{\overline{D_k}^2}{\lambda_s}\right)\right|, \tag{C17}$$

Cloud droplets do not collect snow, but rain drops do. For $k > n_{\text{cloud}}$,

$$\left(\frac{dM_k}{dt}\right)_{\underline{\text{k}}\text{acs}} = \int_0^\infty \frac{\pi}{4}(D_s + \overline{D_k})^2 E_{sk}|U_s(D_s) - U_k|N_k \frac{\pi\rho_s D_s^3}{6}N_{0s}\exp(-\lambda_s D_s)\,dD_s$$
$$= \frac{\pi^2}{24}\rho_s N_{0s}N_k E_{sk} \times \left| a_s\left[\frac{\Gamma(b_s+6)}{\lambda_s^{b_s+6}} + 2\overline{D_k}\frac{\Gamma(b_s+5)}{\lambda_s^{b_s+5}} + \overline{D_k}^2\frac{\Gamma(b_s+4)}{\lambda_s^{b_s+4}}\right] - V_k\left(\frac{120}{\lambda_s^6} + \frac{48\overline{D_k}}{\lambda_s^5} + \frac{6\overline{D_k}^2}{\lambda_s^4}\right)\right|, \tag{C18}$$

where $E_{sk} = 1$. The corresponding bulk quantities are given by

$$\rho_d P_{\text{sacw}} = \sum_{k=1}^{n_{\text{cloud}}}\left(\frac{dM_k}{dt}\right)_{\text{sac}\underline{\text{k}}}, \tag{C19}$$

$$\rho_d P_{\text{sacr}} = \sum_{k=n_{\text{cloud}}+1}^{n_{\text{bin}}}\left(\frac{dM_k}{dt}\right)_{\text{sac}\underline{\text{k}}}, \tag{C20}$$

$$\rho_d P_{\text{racs}} = \sum_{k=n_{\text{cloud}}+1}^{n_{\text{bin}}}\left(\frac{dM_k}{dt}\right)_{\underline{\text{k}}\text{acs}}. \tag{C21}$$

For example, the portions of the unified particle from the coagulation between rainwater and snow become graupel $P_{\text{g.racs}}$. The terms $P_{\text{g.racs}}$, $P_{\text{g.sacr}}$, $P_{\text{s.racs}}$, $P_{\text{s.sacr}}$, $P_{\text{g.sacw}}$, and $P_{\text{s.sacw}}$ are calculated from the above P_{sacw}, P_{sacr}, and P_{racs}. See the references within the tables in appendix A for details of the calculations.

3) Collisions between liquid water and graupel

The collection of cloud droplets by graupel is described in a similar way as the collection by snow. For $k \le n_{\text{cloud}}$,

$$\left(\frac{dM_k}{dt}\right)_{\text{gac}\underline{\text{k}}} = \frac{\pi}{4}N_{0g}M_k E_{gk} \times a_g\frac{\Gamma(b_g+3)}{\lambda_g^{b_g+3}}. \tag{C22}$$

For $k > n_{\text{cloud}}$,

$$\left(\frac{dM_k}{dt}\right)_{\text{gac}\underline{\text{k}}} = \frac{\pi}{4}N_{0g}M_k E_{gk} \times \left| a_g\left[\frac{\Gamma(b_g+3)}{\lambda_g^{b_g+3}} + 2\overline{D_k}\frac{\Gamma(b_g+2)}{\lambda_g^{b_g+2}} + \overline{D_k}^2\frac{\Gamma(b_g+1)}{\lambda_g^{b_g+1}}\right] - V_k\left(\frac{2}{\lambda_g^3} + \frac{2\overline{D_k}}{\lambda_g^2} + \frac{\overline{D_k}^2}{\lambda_g}\right)\right|, \tag{C23}$$

where $E_{gk} = 1$. The corresponding bulk quantities are given by

$$\rho_d P_{\text{gacw}} = \sum_{k=1}^{n_{\text{cloud}}}\left(\frac{dM_k}{dt}\right)_{\text{gac}\underline{\text{k}}}, \tag{C24}$$

$$\rho_d P_{\text{gacr}} = \sum_{k=n_{\text{cloud}}+1}^{n_{\text{bin}}}\left(\frac{dM_k}{dt}\right)_{\text{gac}\underline{\text{k}}}. \tag{C25}$$

REFERENCES

Abel, S. J., and B. Shipway, 2007: A comparison of cloud resolving model simulations of trade wind cumulus with aircraft observation taken during RICO. *Quart. J. Roy. Meteor. Soc.,* **133,** 781–794.

Ackerman, A. S., and Coauthors, 2009: Large-eddy simulations of a drizzling, stratocumulus-topped marine boundary layer. *Mon. Wea. Rev.,* **137,** 1083–1110.

Baba, Y., K. Takahashi, T. Sugimura, and K. Goto, 2010: Dynamical core of an atmospheric general circulation model on a yin–yang grid. *Mon. Wea. Rev.,* **138,** 3988–4005.

Beard, K. V., 1976: Terminal velocity and shape of cloud and precipitation drops aloft. *J. Atmos. Sci.,* **33,** 851–864.

——, and H. T. Ochs, 1984: Collection and coalescence efficiencies for accretion. *J. Geophys. Res.,* **89,** 7165–7169.

——, and ——, 1995: Collisions between small precipitation drops. Part II: Formulas for coalescence, temporary coalescence, and satellites. *J. Atmos. Sci.,* **52,** 3977–3996.

Bigg, E. K., 1953: The supercooling of water. *Proc. Phys. Soc. London,* **B66,** 688–694.

Bott, A., 2000: A flux method for the numerical solution of the stochastic collection equation: Extension to two-dimensional particle distributions. *J. Atmos. Sci.,* **57,** 284–294.

Farley, R. D., and H. D. Orville, 1986: Numerical modeling of hailstorms and hailstone growth. Part I: Preliminary model verification and sensitivity tests. *J. Climate Appl. Meteor.,* **25,** 2014–2035.

Feingold, G., S. Tzivion, and Z. Levin, 1988: Evolution of raindrop spectra. Part I: Solution to the stochastic collection/breakup equation using the method of moments. *J. Atmos. Sci.,* **45,** 3387–3399.

——, R. L. Walko, B. Stevens, and W. R. Cotton, 1998: Simulations of marine stratocumulus using a new microphysical parameterization scheme. *Atmos. Res.,* **47–48,** 505–528.

Grabowski, W. W., and L.-P. Wang, 2008: Diffusional and accretional growth of water drops in a rising adiabatic parcel: Effects of the turbulent collision kernel. *Atmos. Chem. Phys. Discuss.,* **8,** 14 717–14 763.

——, M. Andrejczuk, and L.-P. Wang, 2011: Droplet growth in a bin warm-rain scheme with Twomey CCN activation. *Atmos. Res.,* **99,** 290–301.

Hall, W. D., 1980: A detailed microphysical model within a two-dimensional dynamic framework: Model description and preliminary results. *J. Atmos. Sci.,* **37,** 2486–2507.

Hong, S.-Y., and J.-O. J. Lim, 2006: The WRF single-moment 6-class microphysics scheme (WSM6). *J. Korean Meteor. Soc.,* **42,** 129–151.

Kageyama, A., and T. Sato, 2004: ''Yin-yang grid'': An overset grid in spherical geometry. *Geochem. Geophys. Geosyst.,* **5,** Q09005, doi:10.1029/2004GC000734.

Khain, A. P., and B. Lynn, 2009: Simulation of a supercell storm in clean and dirty atmosphere using weather research and forecast model with spectral bin microphysics. *J. Geophys. Res.,* **114,** D19209, doi:10.1029/2009JD011827.

——, A. Pokrovsky, M. Pinsky, A. Seifert, and V. Phillips, 2004: Simulation of effects of atmospheric aerosols on deep turbulent convective clouds by using a spectral microphysics mixed-phase cumulus cloud model. Part I: Model description and possible applications. *J. Atmos. Sci.,* **61,** 2963–2892.

Khairoutdinov, M., and Y. Kogan, 2000: A new cloud physics parameterization in a large-eddy simulation model of marine stratocumulus. *Mon. Wea. Rev.,* **128,** 229–243.

Kovetz, A., and B. Olund, 1969: The effect of coalescence and condensation on rain formation in a cloud of finite vertical extent. *J. Atmos. Sci.,* **26,** 1060–1065.

Krueger, S. K., C. W. Su, and P. A. McMurtry, 1997: Modeling entrainment and finescale mixing in cumulus clouds. *J. Atmos. Sci.,* **54,** 2697–2712.

Li, X., W.-K. Tao, A. P. Khain, J. Simpson, and D. E. Johnson, 2009: Sensitivity of a cloud-resolving model to bulk and explicit bin microphysical schemes. Part II: Cloud microphysics and storm dynamics interactions. *J. Atmos. Sci.,* **66,** 22–40.

——, ——, T. Matsui, C. Liu, and H. Masunaga, 2010: Improving a spectral bin microphysical scheme using TRMM satellite observations. *Quart. J. Roy. Meteor. Soc.,* **136,** 382–399.

Lim, K.-S. S., and S.-Y. Hong, 2010: Development of an effective double-moment cloud microphysics scheme with prognostic cloud condensation nuclei (CCN) for weather and climate models. *Mon. Wea. Rev.,* **138,** 1587–1612.

Low, T. B., and R. List, 1982a: Collision, coalescence and breakup of raindrops. Part I: Experimentally established coalescence efficiencies and fragment size distributions in breakup. *J. Atmos. Sci.,* **39,** 1591–1606.

——, and ——, 1982b: Collision, coalescence and breakup of raindrops. Part II: Parameterization of fragment size distributions. *J. Atmos. Sci.,* **39,** 1607–1618.

Lynn, B. H., A. P. Khain, J. Dudhia, D. Rosenfeld, A. Pokrovsky, and A. Seifert, 2005: Spectral (bin) microphysics coupled with a mesoscale model (MM5). Part II: Simulation of a CaPE rain event with a squall line. *Mon. Wea. Rev.,* **133,** 59–71.

Milbrandt, J. A., and M. K. Yau, 2005a: A multimoment bulk microphysics parameterization. Part I: Analysis of the role of the spectral shape parameter. *J. Atmos. Sci.,* **62,** 3051–3064.

——, and ——, 2005b: A multimoment bulk microphysics parameterization. Part II: A proposed three-moment closure and scheme description. *J. Atmos. Sci.,* **62,** 3065–3081.

Morrison, H., and J. O. Pinto, 2005: Mesoscale modeling of springtime arctic mixed-phase stratiform clouds using a new two-moment bulk microphysics scheme. *J. Atmos. Sci.,* **62,** 3683–3704.

——, J. A. Curry, M. D. Shupe, and P. Zuidema, 2005: A new double-moment microphysics parameterization for application in cloud and climate models. Part II: Single-column modeling of arctic clouds. *J. Atmos. Sci.,* **62,** 1678–1693.

Nakanishi, M., and H. Niino, 2009: Development of an improved turbulent closure model for the atmospheric boundary layer. *J. Meteor. Soc. Japan,* **87,** 895–912.

Pruppacher, H. R., and J. D. Klett, 1997: *Microphysics of Clouds and Precipitation*. 2nd ed. Kluwer Academic, 954 pp.

Rasmussen, R. M., I. Geresdi, G. Thompson, K. Manning, and E. Karplus, 2002: Freezing drizzle formation in stably stratified layer clouds: The role of radiative cooling of cloud droplets, cloud condensation nuclei, and ice initiation. *J. Atmos. Sci.,* **59,** 837–860.

Reisin, T., Z. Levin, and S. Tzivion, 1996: Rain production in convective clouds as simulated in an axisymmetric model with detailed microphysics. Part I: Description of the model. *J. Atmos. Sci.,* **53,** 497–519.

Reisner, J., R. M. Rasmussen, and R. T. Bruintjes, 1998: Explicit forecasting of supercooled liquid water in winter storms using the MM5 mesoscale model. *Quart. J. Roy. Meteor. Soc.,* **124,** 1071–1107.

Rutledge, S. A., and P. Hobbs, 1983: The mesoscale and microscale structure and organization of clouds and precipitation in midlatitude cyclones. VIII: A model for the ''seeder-feeder'' process in warm-frontal rainbands. *J. Atmos. Sci.,* **40,** 1185–1206.

——, and ——, 1984: The mesoscale and microscale structure and organization of clouds and precipitation in midlatitude cyclones. XII: A diagnostic modeling study of precipitation development in narrow cold-frontal rainbands. *J. Atmos. Sci.,* **41,** 2949–2972.

Sato, Y., T. Nakajima, K. Suzuki, and T. Iguchi, 2009: Application of a Monte Carlo integration method to collision and coagulation growth processes of hydrometeors in a bin-type model. *J. Geophys. Res.,* **114,** D09215, doi:10.1029/2008JD011247.

Shima, S., K. Kusano, A. Kawano, T. Sugiyama, and S. Kawahara, 2009: The super-droplet method for the numerical simulation of clouds and precipitation: A particle-based and probabilistic microphysics model coupled with a non-hydrostatic model. *Quart. J. Roy. Meteor. Soc.,* **135,** 1307–1320.

Shipway, B. J., and A. A. Hill, 2011: The Kinematic Driver Model (KiD). Met Office Tech. Rep. 549, 28 pp.

——, and ——, 2012: Diagnosis of systematic differences between multiple parametrizations of warm rain microphysics

using a kinematic framework. *Quart. J. Roy. Meteor. Soc.,* in press.

Soong, S.-T., 1974: Numerical simulation of warm rain development in an axisymmetric cloud model. *J. Atmos. Sci.,* **31,** 1262–1285.

Srivastava, R. C., 1971: Size distribution of raindrops generated by their breakup and coalescence. *J. Atmos. Sci.,* **28,** 410–415.

Stevens, B., and A. Seifert, 2008: Understanding macrophysical outcomes of microphysical choices in simulations of shallow cumulus convection. *J. Meteor. Soc. Japan,* **86A,** 143–162.

——, G. Feingold, W. R. Cotton, and R. L. Walko, 1996: Elements of the microphysical structure of numerically simulated nonprecipitating stratocumulus. *J. Atmos. Sci.,* **53,** 980–1006.

Straka, J. M., 2009: *Cloud and Precipitation Microphysics: Principles and Parameterizations*. Cambridge University Press, 392 pp.

——, and E. R. Mansell, 2005: A bulk microphysics parameterization with multiple ice precipitation categories. *J. Appl. Meteor.,* **44,** 445–466.

Takahashi, K., X. Peng, K. Komine, M. Ohdaira, K. Goto, M. Yamada, H. Fuchigami, and T. Sugimura, 2005: Nonhydrostatic atmospheric GCM development and its computational performance. *Proc. 11th Workshop on the Use of High Performance Computing in Meteorology,* Reading, United Kingdom, ECMWF, 50–62. [Available online at http://www.ecmwf.int/newsevents/meetings/workshops/2004/high_performance_computing-11th/pdf/Keiko_Takahashi.pdf.]

Thompson, G., R. M. Rasmussen, and K. Manning, 2004: Explicit forecasts of winter precipitation using an improved bulk microphysics scheme. Part I: Description and sensitivity analysis. *Mon. Wea. Rev.,* **132,** 519–542.

——, P. R. Field, R. M. Rasmussen, and W. D. Hall, 2008: Explicit forecasts of winter precipitation using an improved bulk microphysics scheme. Part II: Implementation of a new snow parameterization. *Mon. Wea. Rev.,* **136,** 5095–5115.

Toro, E. F., 1989: A weighted average flux method for hyperbolic conservation laws. *Proc. Roy. Soc. London,* **A423,** 401–418.

Tsias, A., 1996: Ph.D. thesis, Department of Atmospheric Physics, University of Mainz, 193 pp.

Twomey, S., 1959: The nuclei of natural cloud formation. Part II: The supersaturation in natural clouds and the variation of cloud droplets concentrations. *Geofis. Pura Appl.,* **43,** 243–249.

Tzivion, S., G. Feingold, and Z. Levin, 1987: An efficient numerical solution to the stochastic collection equation. *J. Atmos. Sci.,* **44,** 3139–3149.

——, ——, and ——, 1989: The evolution of raindrop spectra. Part II: Collisional collection/breakup and evaporation in a rain shaft. *J. Atmos. Sci.,* **46,** 3312–3328.

van Zanten, M. C., and Coauthors, 2011: Controls on precipitation and cloudiness in simulations of trade-wind cumulus as observed during RICO. *J. Adv. Model. Earth Syst.,* **3,** M06001, doi:10.1029/2011MS000056.

Wacker, U., and A. Seifert, 2001: Evolution of rain water profiles resulting from pure sedimentation: Spectral vs. parameterized description. *Atmos. Res.,* **58,** 19–39.

Wicker, L. J., and W. C. Skamarock, 2002: Time-splitting methods for elastic models using forward time schemes. *Mon. Wea. Rev.,* **130,** 2088–2097.

Young, K. C., 1975: The evolution of drop spectra due to condensation, coalescence and breakup. *J. Atmos. Sci.,* **32,** 965–973.